IEEE Access
Multidisciplinary ⋮ Rapid Review ⋮ Open Access Journal

Received 11 August 2022, accepted 29 September 2022, date of publication 10 October 2022, date of current version 14 October 2022.

Digital Object Identifier 10.1109/ACCESS.2022.3213034

RESEARCH ARTICLE

Comparison of Various Hybrid Electric Powertrains for Non-Road Mobile Machinery Using Real-Time Multibody Simulation

GIOTA GOSWAMI[1], ANNA TUPITSINA[2], SURAJ JAISWAL[1], CHARLES NUTAKOR[1], TUOMO LINDH[2], AND JUSSI SOPANEN[1], (Member, IEEE)

[1]Department of Mechanical Engineering, Lappeenranta-Lahti University of Technology—LUT, 53850 Lappeenranta, Finland
[2]Department of Electrical Engineering, Lappeenranta-Lahti University of Technology—LUT, 53850 Lappeenranta, Finland

Corresponding author: Giota Goswami (giota.goswami@lut.fi)

This work was supported by Business Finland under the e3Power Project (http://e3power.fi/).

ABSTRACT Electrification of non-road mobile machinery holds immense potential for reducing the high emissions and fuel consumption of such industrial machinery. Detailed real-time physics-based simulation models capable of comparing energy efficiencies of hybrid powertrains in realistic working conditions can aid the development of efficient mobile machinery. In this study, four system-level hybrid electric powertrain models have been developed and coupled with a detailed multibody dynamics-based tractor model in a co-simulation environment. The four models, differentiated by their topology and transmission design, are simulated in a virtual environment under the dynamic load conditions of a ploughing work cycle of the Deutsche Landwirtschafts-Gesellschaft powermix. The simulation results show that improvements of 9.7% and 9.2% in total energy consumption can be achieved by the two studied power-split configurations in the simulated work cycle compared to an automated manual transmission-based series powertrain. The double planetary gear-based power-split model achieved the highest energy recovery and lowest energy loss compared to the other models. The developed models are real-time capable, allowing a human operator to simulate customizable work cycles.

INDEX TERMS Hybrid electric vehicle, power transmission, tractor model, multibody dynamics, driveline simulation.

I. INTRODUCTION

Hybrid electric vehicles (HEVs) represent only a small fraction of vehicles used worldwide despite their tremendous sales growth in the last decade [1]. With growing concerns for the environment, tightening CO_2 emission regulations, and various fuel economy initiatives, the demand for energy-efficient powertrains has increased greatly in recent years. In practice, a prototype-based development of such hybrid electric powertrains may be expensive or cumbersome [2]. However, they can be modeled to investigate energy-efficient solutions for non-road mobile machinery (NRMM) in the framework of detailed real-time multibody simulation. This can allow vehicle manufacturers to test various powertrain models using computer simulations before building a physical prototype. Moreover, the physics-based real-time simulation model can be utilized in user training, research, and various product process [3], [4].

The development of flexible and configurable simulation models to evaluate the energy efficiency of HEV powertrains has been the focus of much research and many studies have focused on hybrid powertrain configurations with the aim of improving fuel efficiency [5], [6], [7], [8]. For example, the dual-mode power-split transmission proposed for HEVs in [9] was shown to improve fuel economy and reduce emissions significantly. The method proposed in [10] optimized the design of the transmission of a single shaft plug-in HEV, and the selection of gear ratios, resulting in an improvement in fuel economy by about 3% compared to the current transmission design. A topology optimization

The associate editor coordinating the review of this manuscript and approving it for publication was Ali Raza.

method was proposed in [11] for selection of the optimal configuration of a HEV based on comparing two transmissions – an automated manual transmission (AMT) and a continuously variable transmission (CVT). The approach achieved relative CO_2 emission reductions of between 2% and 8%. Similarly, control strategies have been developed and used in hybrid powertrain simulations to achieve increased fuel economy and enhanced performance [12], [13], [14], [15]. The control of energy management and gear-shifting based on dynamic particle swarm optimization strategy presented in [16] resulted in fuel savings upto about 31%. In [17], the operating points of the motor were manipulated using a variable transmission and it was found that the drivetrain losses outweigh the efficiency gained in the motor.

The above studies show how computer simulations are widely used to investigate possible improvements in powertrain design. It should be noted, however, that the majority of the work has focused exclusively on passenger vehicles [18] and NRMM have received relatively little attention. Hybrid construction machinery has entered the market in the past decade, and there remains potential for notable market expansion [19]. Due to the growing global understanding of the advantages of HEVs, there has been an increase in hybridization of many powertrains for applications other than passenger vehicles. Therefore, the electrification of NRMM with distinctive work cycles has started recently [20].

Energy efficiency studies of NRMM show that there is considerable potential for improvement in fuel economy through improved powertrain design. The comparative energy efficiencies and life cycle costs of a conventional, hybrid, and fuel cell powertrain for an underground mining loader were evaluated in [21] and the simulations showed increased fuel economy of almost 30% and 50% for the hybrid electric loader and the fuel cell hybrid, respectively, when compared to a conventional loader. Four hybrid electric powertrain configurations for agricultural tractors were proposed in [22], finding the highest fuel savings in the series configuration and superior peak power performance in the parallel configuration. A series hybrid electric powertrain with a hybrid energy storage and multi-speed transmission was investigated for a military tracked vehicle in [23] achieving about 30% improvement in fuel economy compared to a conventional series hybrid configuration. The series, parallel, and compound hybrid configurations of an excavator were simulated in [24] and a control algorithm proposed, which was shown to achieve 20% reduced fuel consumption compared to a conventional hydraulic excavator. A multi-mode power-split hybrid electric powertrain for tracked vehicles using three planetary gears was proposed in [25] and shown to achieve 30% improvement in drivability and a 15% improvement in fuel economy compared to a conventional series hybrid configuration.

The work cycles for different NRMM vary largely and are often not accurately known beforehand. Most of the above studies utilized two-dimensional longitudinal models of the vehicle, which cannot describe the detailed vehicle dynamics. In passenger vehicles where the drive cycles are intended for transportation, the high-level approach of longitudinal dynamics is sufficient for energy analyses. However, in the field cycles of NRMM working conditions, detailed vehicle dynamics are vital for energy analyses, especially, in complicated scenarios like excavation, compaction, bucket loading and cultivation. Such dynamic loading scenarios for NRMM cannot be comprehensively described by longitudinal models which are prevalent in existing literature [21], [22], [23]. Such scenarios require a human operator simulating customizable work cycles that are not pre-determined. For this reason, some studies have adopted detailed physics-based models of HEVs. For example, a multibody chassis model capable of studying the effects of hybrid electric powertrains on ride and handling was developed and validated using a test vehicle in [26]. A torque vectoring control strategy was proposed in [27] and its performance was assessed by applying it to a multibody dynamics-based HEV. The simulation results showed that improved vehicle response and drivability were achieved by the controller. A vibration controller was developed in [28] with a longitudinal vehicle model whose simulation results were validated using a multibody vehicle model. An experimental and numerical analysis of vibrations caused by engine starts in a power-split HEV was studied in [29] where the full vehicle, including the driveline and the suspension, were modeled using a multibody approach. A real-time multibody simulation-based underground mining loader was presented in [30] to couple a series hybrid powertrain in a co-simulation platform. Using the co-simulation platform, the energy consumption of the loader was studied in its natural working environment. This study was extended in [31] to compare the series hybrid electric loader with a conventional diesel-powered machine, and a reduction in fuel consumption of 34% to 56% was found [31]. The above studies show that detailed physics-based models can improve energy efficiency studies by accounting for the complex vehicle dynamics, and also allow various other studies, such as ride, handling and drivability, which are relevant in case of hybrid electric NRMM.

Despite considerable previous research efforts on HEVs, powertrain efficiency and vehicle dynamics as discussed above, there are certain gaps in the existing literature. First, even though studies on HEVs provide detailed explanations of various powertrain configurations and designs, detailed vehicle dynamics, which are crucial for NRMM simulations, have been neglected. Second, even though the literature on detailed physics-based real-time simulation of HEVs includes hybrid electric powertrains, a thorough investigation on various possible powertrains and transmission designs has been overlooked. This study aims to fill these research gaps by proposing a simulation methodology and environment that can combine and investigate various system-level hybrid electric powertrains with a detailed real-time physics-based model of NRMM. Such simulations can capture the complex functions and dynamics of NRMM while allowing human

operators to simulate standardized and customizable NRMM work cycles.

The objective of this paper is to introduce and compare different system-level hybrid electric powertrain models within the framework of detailed real-time multibody simulation of NRMM. The study considers four configurations – an AMT-based series configuration, a CVT-based series configuration, a single planetary gear power-split configuration, and a double planetary gear power-split configuration. All four models utilize a similar diesel engine, generator, battery, and electric motor. As a case example, a tractor is modeled using a semi-recursive multibody formulation [32] describing accurate and detailed vehicle dynamics. The tires are modeled using the lumped LuGre tire model [33], [34] and a deformable terrain environment is modeled using a combined mesh-based [35], [36] and particle-based [37], [38] method. The hybrid electric powertrain models of the tractor are evaluated based on the electric motor and diesel engine power, battery state of charge, fuel consumption, energy consumption, and real-time capability in a three-dimensional maneuver of a ploughing work cycle from the German Agricultural Society (Deutsche Landwirtschafts-Gesellschaft–DLG) [39].

This paper contains six sections. The rest of the paper is organized such that Sect. II describes hybrid electric powertrain and Sect. III describes multibody modeling. The case study of a tractor is described in Sect. IV, while results and discussion are presented in Sect. V and a conclusion is provided in Sect. VI.

II. HYBRID POWERTRAIN MODELING

The topologies of hybrid powertrains commonly used in NRMM applications are series, parallel, and series-parallel. In the series configuration, there is no direct connection between the diesel engine and the transmission. While this provides the benefit of allowing the engine to always operate at its highest efficiency point, it also introduces the downside that the motor, being the sole energy provider for the vehicle propulsion, must have a power rating that meets the vehicle's requirements [40]. In this study, two series hybrid powertrain models using an AMT and a CVT are developed. The series AMT model serves as the benchmark configuration with which the other models are compared. The parallel topology, on the other hand, allows flexibility in choosing the size of the motor. It is also favored by manufacturers as only minor changes are required in existing vehicles to switch to this configuration. However, in a hybrid powertrain with parallel topology, charging is only possible when the vehicle is moving, making it unsuitable for driving cycles involving frequent stops [40]. The series-parallel topology combines the two topologies to benefit from the strengths of each topology while eliminating the drawbacks. Two power-split configurations based on the series-parallel topology are developed in this work. All the powertrain models developed in this work use a rule-based control strategy and are compared with the series AMT benchmark configuration to study the energy efficiency of hybrid electric powertrains in NRMM applications.

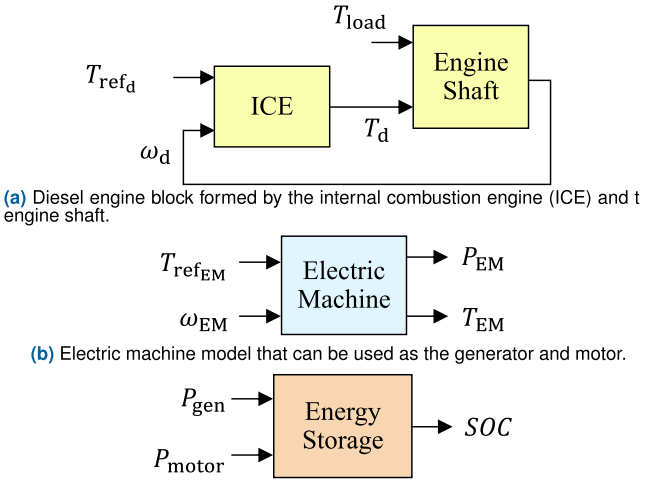

(a) Diesel engine block formed by the internal combustion engine (ICE) and t engine shaft.

(b) Electric machine model that can be used as the generator and motor.

(c) Energy storage model that acts as the secondary energy source.

FIGURE 1. Components of the diesel-electric drive.

A. DIESEL-ELECTRIC DRIVE

The powertrain of the HEV consists of a diesel engine, an electric machine, energy storage, and its auxiliary systems. These components are modeled in a modular way for the convenience of standalone changes in each element and to enable different coupling according to the configuration type. The modeling block of each component reflects the power flow in the component as shown in Fig. 1. The internal combustion engine (ICE) takes the reference torque (T_{ref_d}) and the torque load on the engine shaft (T_{load}) as inputs and calculates the torque (T_d) and the rotational speed (ω_d) of the diesel engine as outputs. The electric machine takes the reference torque ($T_{ref_{EM}}$) and the rotational speed of the electric machine (ω_{EM}) as inputs and calculates the electric machine torque (T_{EM}) and power (P_{EM}) as outputs. The battery uses the generator power input (P_{gen}) and motor power input (P_{motor}) to calculate the battery state of charge (SOC) as output.

The primary energy source in a NRMM is the diesel engine. The engine is modeled using a maximum torque curve and an efficiency map as shown in Fig. 2. The engine's dynamics are modeled using a first-order transfer function. The reference torque required from the engine is determined by the controller. This required torque of the engine is limited by the maximum torque curve and delayed by the first-order transfer function to obtain the actual engine torque. The fuel consumption can be calculated as [41]:

$$FC = \frac{T_d\,\omega_d}{E_J\,\eta_d(T_d, \omega_d)}, \tag{1}$$

where E_J is the fuel heat value, ω_d is the rotational speed of the diesel engine, and $\eta_d(T_d, \omega_d)$ is the efficiency of the diesel engine found from the efficiency map (Fig. 2) corresponding to T_d and ω_d. The fuel heat value is taken as 43 MJ/kg in this work.

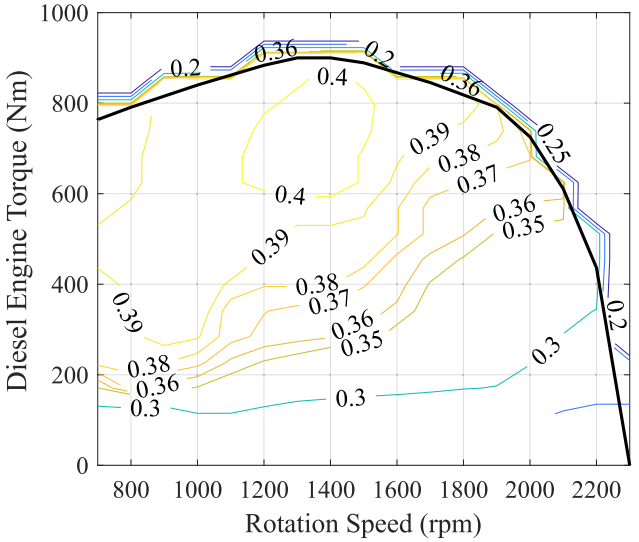

FIGURE 2. Efficiency map of the diesel engine.

When the diesel engine and generator are mounted on the same shaft, the rotational speed of the shaft can be calculated as:

$$\omega_{\mathrm{d}} = \int \frac{T_{\mathrm{d}} - T_{\mathrm{load}}}{J_{\mathrm{d}}} dt, \tag{2}$$

where J_{d} is the rotational inertia of the diesel engine genset and T_{load} is the torque load on the shaft which corresponds to the generator torque.

An electric machine can be represented by dynamical or quasi-static models. The dynamical model employs the space vector theory in a two-dimensional coordinated system, which reflects the fast transients of the machine. However, it requires complicated calculations and increases the computation time needed for multiple machine systems. The quasi-static approach uses efficiency maps to reflect losses in the electric machine. This method provides an opportunity to reduce computational time while achieving sufficient accuracy for modeling of HEV systems [42]. The quasi-static approach was therefore utilized in this work. In this approach, the efficiency map is coupled with the maximum torque curve, shown in Fig. 3a, and a first-order transfer function to limit the changes in torque. The electric machine is controlled by a frequency inverter, whose losses are also modeled using an efficiency map shown in Fig. 3b.

The data for the efficiency maps of the electrical components can be obtained from the manufacturer or through measurements. The diesel engine efficiency map can be obtained by various methods such as the calculation tool introduced in [43]. The electric machine and its inverter power input which is flowing to or from the battery can be expressed as:

$$P_{\mathrm{EM}} = \begin{cases} \dfrac{P_{\mathrm{load}}}{\eta_{\mathrm{EM}}} = \dfrac{T_{\mathrm{EM}}\,\omega_{\mathrm{EM}}}{\eta_{\mathrm{EM}}(T_{\mathrm{EM}}, \omega_{\mathrm{EM}})} & P_{\mathrm{EM}} \geq 0, \\ P_{\mathrm{load}}\,\eta_{\mathrm{EM}} = T_{\mathrm{EM}}\,\omega_{\mathrm{EM}}\,\eta_{\mathrm{EM}}(T_{\mathrm{EM}}, \omega_{\mathrm{EM}}) & P_{\mathrm{EM}} < 0, \end{cases} \tag{3}$$

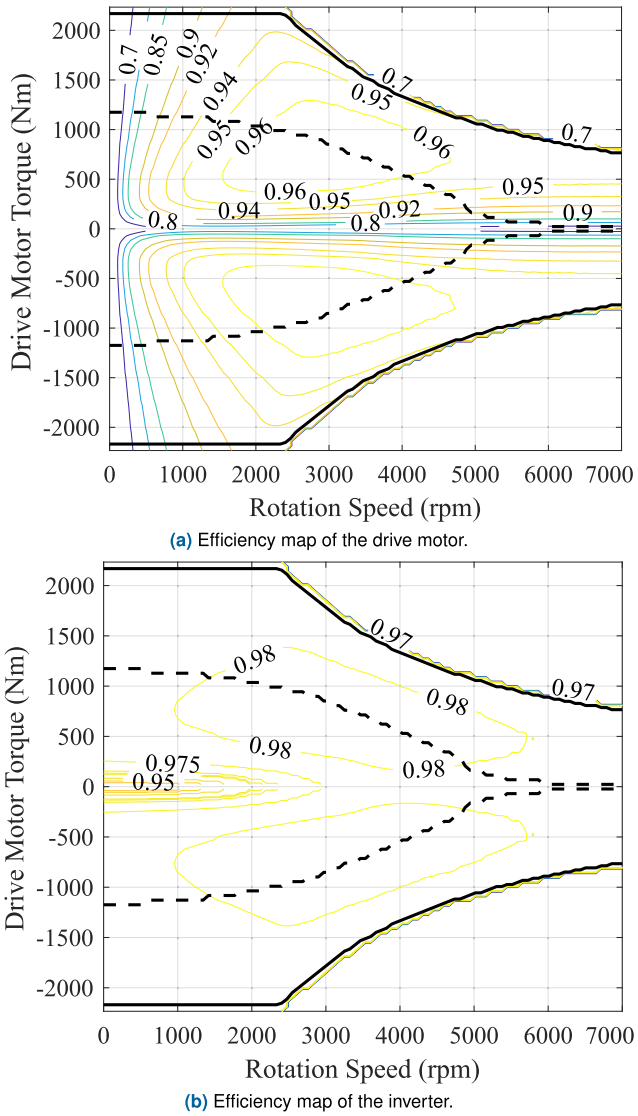

(a) Efficiency map of the drive motor.

(b) Efficiency map of the inverter.

FIGURE 3. Maps used to obtain the efficiencies of the electric motor and inverter.

where P_{load} is the power output of the electric machine, and $\eta_{\mathrm{EM}}(T_{\mathrm{EM}}, \omega_{\mathrm{EM}})$ is the efficiency of the electric machine and inverter combined. The motor power loss is the difference between the input and output powers of the motor which can be calculated as:

$$P_{\mathrm{loss}} = P_{\mathrm{EM}} - P_{\mathrm{load}}. \tag{4}$$

The secondary energy source is energy storage which is a battery. The modeling of the battery is based on the Simscape Electrical battery model described by Shepherd equations [44]. The model describes a generic dynamic of a rechargeable battery. The battery's voltage at the output terminals can be calculated as: (5) and (6), shown at the bottom of the next page. where E_0 is the constant voltage value taken as 2.5466 V, R is the internal resistance taken as 0.000355 Ohm, I_{bat} is the battery current taken as 4 A, E_{bat} is the voltage at the output terminals, K is the polarization constant/polarization resistance taken as 4.3891e-04, $Q_{\max}$ is

the maximum battery capacity taken as 20 Ah, i_{bat*} is the filtered current, A is the exponential zone amplitude taken as 0.2034 V, and B is the exponential zone time constant inverse taken as 6.1142. The maximum current that can be drawn from the battery is 900 A. These parameters are extracted from the manufacturer-provided discharge curve and datasheet. The actual charge, Q, can be expressed as:

$$Q = (1 - SOC_{\text{init}})Q_{\max} + \int \frac{I_{\text{bat}}}{3600} dt. \tag{7}$$

Using the modified Coulomb counting method, the SOC can be estimated as:

$$SOC = SOC_{\text{init}} + \int \frac{I_{\text{bat}}}{3600 Q_{\max}} dt, \tag{8}$$

where SOC_{init} is the initial SOC. The battery is connected directly to the DC link without a DC/DC converter.

B. TRANSMISSION

The types of transmissions used in this study include automated manual transmission (AMT), continuously variable transmission (CVT) and planetary gearsets. These gearboxes typically consist of clutches, simple gears, belt and pulley drives, coupling devices and power-split devices. Disc friction clutches are used in transmissions to engage the required gears. In the case of AMT, the gears are selected based on the vehicle velocity by providing an actuation pressure to the corresponding clutches. The frictional torque of a clutch can be written as [45]:

$$T_{\text{cl}} = \mu_{\text{cl}}\, n\, r_{\text{eff}} P A_{\text{cl}}, \tag{9}$$

where μ_{cl} is the coefficient of friction of the clutch plate, n is the number of friction surfaces, r_{eff} is the effective torque radius, P is the engagement pressure, and A_{cl} is the engagement surface area. The clutch is unlocked when the clutch torque is zero, slipping when the clutch torque is above zero but less than the input torque and locked when the clutch torque reaches the input torque [45]. The gears allow transmission based on each gear's transmission ratio such that:

$$\omega_{\text{in}} = i\omega_{\text{pt}}, \tag{10}$$

$$T_{\text{pt}} = \begin{cases} i\, T_{\text{in}}\, \eta_{\text{g}} & T_{\text{in}} \geq 0, \\ i\, \dfrac{T_{\text{in}}}{\eta_{\text{g}}} & T_{\text{in}} < 0, \end{cases} \tag{11}$$

where ω_{in} is the speed input to the gear, i is the gear ratio, ω_{pt} is the speed output from the gear or powertrain, η_{g} is the transmission efficiency, T_{pt} is the torque output from the gear or powertrain and T_{in} is the torque input to the gear.

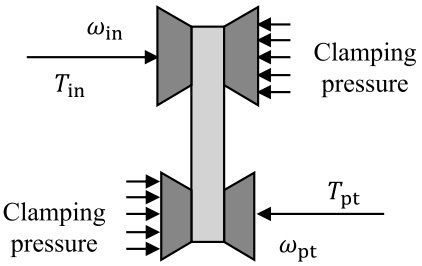

FIGURE 4. A continuously variable transmission (CVT) which consists of a belt and pulley drive.

While simple gears allow switching between fixed gear ratios, belt and pulley drives vary the transmission ratio continuously using a belt over two pulleys of variable diameter kept apart by a fixed distance as shown in Fig. 4. In belt and pulley CVTs the pitch radii of the pulleys can be controlled by a variator which applies a clamping pressure on the movable pulley sheaves. The power transmission in the belt and pulley drive can also be expressed by Eqs. (10) and (11).

The CVT introduces the advantage of selecting the transmission ratio based on the demanded power. In a series powertrain the power management control strategy typically aims to operate the engine in its high efficiency region while the motor provides for the entire traction demand. In this study, the CVT variator is designed to operate the motor at a relatively high efficiency, which is achieved using the motor and inverter efficiency map shown in Fig. 3. The low-speed region from 0 to 1000 revolutions per minute (rpm) covers the lowest efficiencies. The variator selects the speed ratio such that this region is avoided while the motor is running.

Power-split devices typically consist of one or more planetary gears – and example is shown in Fig. 5 – depending on the number of modes required. The planet carrier, sun and ring gears of the planetary gear can be connected to the engine, generator and transmission in such a configuration that the inputs or outputs from the different energy sources in the powertrain can be split. The kinematic constraints and torque relations of a planetary gear can be written as:

$$r_{\text{C}}\omega_{\text{d}} = r_{\text{S}}\omega_{\text{S}} + r_{\text{P}}\omega_{\text{P}}, \tag{12}$$

$$r_{\text{R}}\omega_{\text{R}} = r_{\text{C}}\omega_{\text{d}} + r_{\text{P}}\omega_{\text{P}}, \tag{13}$$

$$T_{\text{S}} = \begin{cases} \dfrac{r_{\text{S}}}{r_{\text{R}}} T_{\text{R}} \eta_{\text{RS}} & T_{\text{R}} \geq 0, \\ \dfrac{r_{\text{S}} T_{\text{R}}}{r_{\text{R}} \eta_{\text{RS}}} & T_{\text{R}} < 0, \end{cases} \tag{14}$$

$$T_{\text{C}} + T_{\text{R}} + T_{\text{S}} = 0, \tag{15}$$

$$V_{\text{bat}} = E_0 - R I_{\text{bat}}, \tag{5}$$

$$E_{\text{bat}} = \begin{cases} V_{\text{bat}} - \dfrac{KQ_{\max}}{Q_{\max} - Q} Q - \dfrac{KQ_{\max}}{Q_{\max} - Q} i_{\text{bat}*} + A e^{BQ} & i_{\text{bat}*} \geq 0, \\ V_{\text{bat}} - \dfrac{KQ_{\max}}{Q_{\max} - Q} Q - \dfrac{KQ_{\max}}{Q + 0.1Q_{\max}} i_{\text{bat}*} + A e^{BQ} & i_{\text{bat}*} < 0, \end{cases} \tag{6}$$

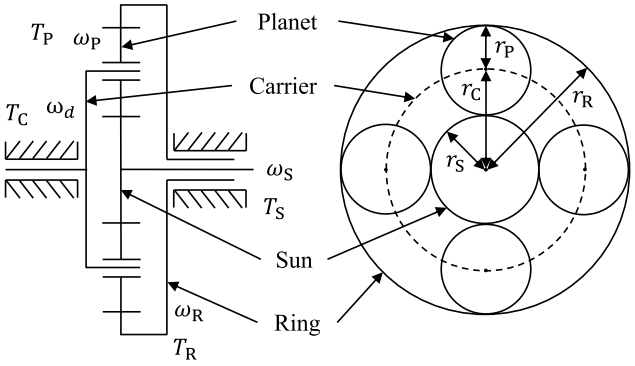

FIGURE 5. Schematic of planetary gearset which consists of a sun, four planets, a planet carrier and a ring.

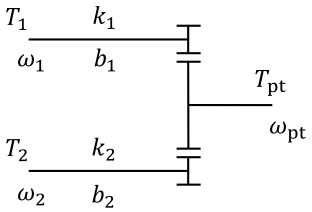

FIGURE 6. A coupling device merging the torques of two shafts.

where r_C is the radius of the carrier, ω_d is the angular velocity of the carrier which is the angular velocity of the diesel engine connected to it, T_C is the torque of the carrier, r_S is the radius of the sun, ω_S is the angular velocity of the sun, T_S is the torque of the sun, r_P is the radius of the planet, ω_P is the angular velocity of the planet, r_R is the radius of the ring, ω_R is the angular velocity of the ring, T_R is the torque of the ring, and η_{RS} is the efficiency of power transfer between the ring and the sun. When the diesel engine and generator are connected to the planetary gear, the engine rotational speed is calculated using the kinematic constraints Eq. (12) and Eq. (13) instead of Eq. (2).

Coupling devices are required in transmissions for parallel or series-parallel hybrids to couple the power parallelly transmitted from the different power sources. In a gear coupling as shown in Fig. 6, the torque and angular velocities of the shafts can be expressed as:

$$T_{pt} + T_1 + T_2 = 0, \tag{16}$$

$$T_1 = (\omega_{pt} - \omega_1)b_1 - \theta_1 k_1, \tag{17}$$

$$T_2 = (\omega_{pt} - \omega_2)b_1 - \theta_2 k_2, \tag{18}$$

where T_{pt} is the torque of the output shaft or the powertrain, ω_{pt} is the angular velocity of the output shaft or the powertrain, T_1 is the torque of the first input shaft, ω_1 is the angular velocity of the first input shaft, T_2 is the torque of the second input shaft, ω_2 is the angular velocity of the second input shaft, θ_1 is the rotation angle of the first shaft, θ_2 is the rotation angle of the second shaft, b_1 is the viscous damping coefficient of the first shaft, b_2 is the viscous damping coefficient of the second shaft, k_1 is the torsional stiffness of the first shaft and k_2 is the torsional stiffness of the second shaft.

C. CONTROL STRATEGY

Rule-based supervisory control can be implemented in real-time without prior information about the work cycle with realistic switching of modes using actuators [46]. Therefore, due to its effectiveness in real-time implementation a simple rule-based controller has been used in this work to demonstrate the capability of the developed models to simulate and compare control strategies. The heuristic mode change logic of the control strategy, shown in Fig. 7, is based on operating the diesel engine in a high-efficiency region obtained from the efficiency map (Fig. 2).

The parameters used in the rules are the minimum generated power of the diesel engine (P_{d_min}), the lower and upper limits of battery state of charge (SOC_{low} and SOC_{upp}), the maximum battery power (P_{b_max}) and the optimal diesel power (P_{d_opt}). These are tunable parameters which have been set according to the diesel engine efficiency map in this study. The controller takes the motor power output (P_{load}) and the battery state of charge (SOC) as inputs to decide the power to be supplied by the diesel engine. The engine reference torque (T_{ref_d}) is determined by looking up high efficiency regions from the efficiency map corresponding to the decided engine power. The engine speed is regulated by controlling the generator torque or speed. When the engine and generator are mounted on the same shaft, they share the same speed which can be regulated by controlling the generator torque (Eq. (2)). When the engine and generator are connected to the different shafts of the planetary gear, the engine speed can be regulated by controlling the generator speed (Eq. (12) and Eq. (13)) [46].

The following three modes have been defined for the controller in this study, based on the constant and instantaneous parameters mentioned above:

1) Battery mode – This mode is used when the battery has a high amount of charge available, and the traction demand is low. When the $SOC > SOC_{upp}$ and $P_{load} < P_{d\_min}$, the engine is run at the minimum power until the SOC drops below its lower limit or the motor power exceeds P_{b_max}.
2) Hybrid mode – This mode is used when the battery requires charging. The engine provides a constant power P_{d_opt} to replenish the battery charge. When the battery charge rises above its upper limit and the motor power is low, control can be switched back to the battery mode. If, on the other hand, the motor power exceeds P_{b_max}, then the control is switched to the max mode.
3) Max mode – This mode is used when there is a high traction demand. The engine tries to match the motor power in this mode so that the battery charge can be replenished and, in case of series-parallel configurations, the motor can be assisted in fulfilling the traction demand. When the motor power is lower than P_{b_max} the control is switched back to the hybrid mode.

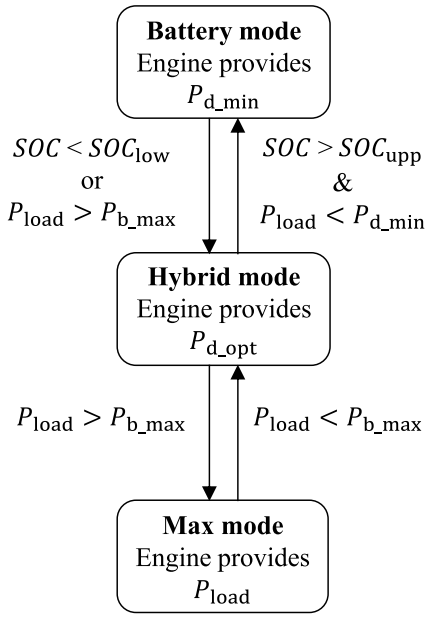

FIGURE 7. Mode change logic of the rule-based supervisory control strategy showing the conditions under which the modes are switched.

III. MULTIBODY SYSTEM DYNAMICS

The multibody approach can be used to model the detailed dynamics of various NRMM like excavators [47], wheel loaders [48], forklifts [48], tree harvesters [49] and underground mine loaders [30]. This approach allows the modeling of the details in various NRMM that distinguish their operations and working environments from each other. The equations of motion of a NRMM can be described using a semi-recursive multibody formulation [32]. By using a multibody approach, multiple bodies, tires, and a realistic environment can be modeled even in a real-time framework [47], [50]. The tires in this study are modeled using the lumped LuGre tire model [33], [34]. The deformable terrain is modeled using a combination of mesh-based [35], [36] and particle-based methods [37].

A. SEMI-RECURSIVE MULTIBODY FORMULATION

The dynamics of mechanical components of a NRMM such as a tractor are described using a semi-recursive multibody formulation [32]. Here, the equations of motion are formulated first in the Cartesian coordinates and then switched to the relative joint coordinates using a velocity transformation matrix [51]. Here, the center of mass of a body is chosen as the reference point. The dynamics of closed-loop models are formulated by incorporating loop-closure constraints in the dynamics of its equivalent open-loop model.

Consider a tree-structure open-loop model with N_b rigid bodies with any number of branches. The model kinematics can be recursively expressed from the base to the leaves using the classical kinematic relations [32]. Using the principle of virtual work, the virtual power of the forces acting on an open-loop model can be written as [32], [52]:

$$\delta\dot{\mathbf{q}}^{*\mathrm{T}}\left(\mathbf{M}\ddot{\mathbf{q}}-\mathbf{Q}\right)=\mathbf{0}, \tag{19}$$

where $\dot{\mathbf{q}} \in \mathbb{R}^{6N_b}$ and $\ddot{\mathbf{q}} \in \mathbb{R}^{6N_b}$ are the vectors of Cartesian velocities and accelerations, respectively; an asterisk (*) denotes the virtual velocities that are assumed to be kinematically admissible; $\mathbf{M} \in \mathbb{R}^{6N_b\times 6N_b}$ is the mass matrix; and $\mathbf{Q} \in \mathbb{R}^{6N_b}$ is the external force and torque vector. Using a velocity transformation matrix $\mathbf{R} \in \mathbb{R}^{6N_b\times N_b}$, the Cartesian velocities are mapped onto the relative joint velocities as [51]:

$$\dot{\mathbf{q}}=\mathbf{R}\dot{\mathbf{z}}, \tag{20}$$

$$\ddot{\mathbf{q}}=\mathbf{R}\ddot{\mathbf{z}}+\dot{\mathbf{R}}\dot{\mathbf{z}}, \tag{21}$$

where $\dot{\mathbf{z}} \in \mathbb{R}^{N_b}$ and $\ddot{\mathbf{z}} \in \mathbb{R}^{N_b}$ are the relative joint velocity and acceleration vectors, respectively, and the term $\dot{\mathbf{R}}\dot{\mathbf{z}}$ are the Cartesian accelerations computed with true relative joint velocities and zero relative joint accelerations. Using Eqs. (20) and (21) in Eq. (19), the equations of motion of the open-loop model can be written as:

$$\mathbf{R}^{\mathrm{T}}\mathbf{M}\mathbf{R}\ddot{\mathbf{z}}=\mathbf{R}^{\mathrm{T}}\left(\mathbf{Q}-\mathbf{M}\dot{\mathbf{R}}\dot{\mathbf{z}}\right), \tag{22}$$

which represents N_b numbers of ordinary differential equations. In this study, the rows of matrix $\mathbf{R}$ that affects each body are computed in parallel using the body-by-body technique as in [51].

For a closed-loop model, the loop-closure constraints are incorporated in the open-loop dynamics using the penalty method [53] as in [51]. Accordingly, the equations of motion of the closed-loop model can be written as:

$$\left(\mathbf{M}^{\Sigma}+\boldsymbol{\Phi}_{\mathbf{z}}^{\mathrm{T}}\boldsymbol{\alpha}\boldsymbol{\Phi}_{\mathbf{z}}\right)\ddot{\mathbf{z}} = \mathbf{Q}^{\Sigma}-\boldsymbol{\Phi}_{\mathbf{z}}^{\mathrm{T}}\boldsymbol{\alpha}\left(\dot{\boldsymbol{\Phi}}_{\mathbf{z}}\dot{\mathbf{z}}+2\boldsymbol{\Omega}\boldsymbol{\mu}\boldsymbol{\Phi}_{\mathbf{z}}\dot{\mathbf{z}}+\boldsymbol{\Omega}^{2}\boldsymbol{\Phi}\right), \tag{23}$$

where $\boldsymbol{\Phi}$ are the constraint equations, $\boldsymbol{\Phi}_{\mathbf{z}}$ is its Jacobian matrix, $\dot{\boldsymbol{\Phi}}_{\mathbf{z}}$ is the partial derivative of $\boldsymbol{\Phi}_{\mathbf{z}}$ with respect to time, $\boldsymbol{\alpha}$, $\boldsymbol{\Omega}$, and $\boldsymbol{\mu}$ are the diagonal matrices containing values of the penalty factors, natural frequencies, and damping ratios, respectively, $\mathbf{M}^{\Sigma}=\left(\mathbf{R}^{\mathrm{T}}\mathbf{M}\mathbf{R}\right)$, and $\mathbf{Q}^{\Sigma}=\left[\mathbf{R}^{\mathrm{T}}\left(\mathbf{Q}-\mathbf{M}\dot{\mathbf{R}}\dot{\mathbf{z}}\right)\right]$. Note that the constraints are assumed to be holonomic and scleronomic.

B. TIRE MODEL

In this study, tires are described using the lumped LuGre tire model [33], [34] as shown in Fig. 8. The tires are assumed as a series of discs subject to longitudinal, vertical, and lateral forces. It should be noted that high-fidelity tire-soil interaction has been ignored in this study because it would lead to heavy computational load making the model unsuitable for real-time simulation [54]. The lumped LuGre tire model is an extension of the Dahl model [55] incorporating the stiction and Stribeck effects [56]. The lumped LuGre tire model can be written as:

$$\dot{\bar{\mathbf{z}}}=\mathbf{v}_{\mathrm{t}}-\frac{\sigma_0\left|\mathbf{v}_{\mathrm{t}}\right|}{g(\mathbf{v}_{\mathrm{t}})}\bar{\mathbf{z}}, \tag{24}$$

$$g(\mathbf{v}_{\mathrm{t}})=\mu_{\mathrm{c}}+(\mu_{\mathrm{s}}-\mu_{\mathrm{c}})\,e^{-\left(\frac{|\mathbf{v}_{\mathrm{t}}|}{v_{\mathrm{s}}}\right)^{\frac{1}{2}}}, \tag{25}$$

$$\mathbf{F}_{\mu}=\left(\sigma_0\bar{\mathbf{z}}+\sigma_1\dot{\bar{\mathbf{z}}}+\sigma_2\mathbf{v}_{\mathrm{t}}\right)\mathbf{F}_{\mathrm{n}}, \tag{26}$$

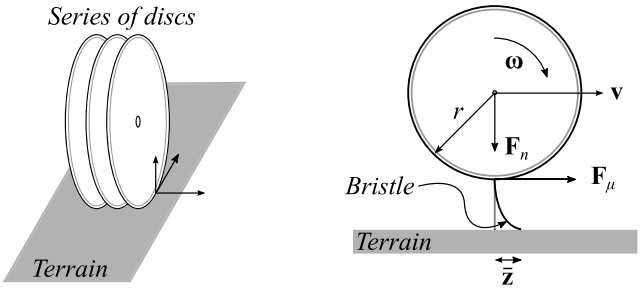

FIGURE 8. Illustration of a tire model.

where $\bar{\mathbf{z}}$ is the average bristle deflection vector, σ_0 and σ_1 are the stiffness and damping of the elastic bristles, respectively, $\mathbf{v}_t$ is the relative tangential velocity vector, v_s is the Stribeck velocity, μ_c and μ_s are the respective coefficients of the Coulomb and static friction, σ_2 is the coefficient of viscous friction, $\mathbf{F}_\mu$ is the friction force, and $\mathbf{F}_n$ is the normal force. Here, $|\mathbf{v}_t| = r\,|\boldsymbol{\omega}| - |\mathbf{v}|$, with r, $\boldsymbol{\omega}$, and $\mathbf{v}$ being the radius, angular velocity, and linear velocity of a tire, respectively.

C. DEFORMABLE TERRAIN MODEL

In this study, the deformable terrain is modeled by combining the mesh-based [35], [36] and particle-based methods as in [38]. In the mesh-based method, the terrain is defined as cells in a grid (a heightfield) allowing the formation of a landscape. The heightfield is split into vertical slices such that the pressure over the base of a cell is a combination of pressures from its own block and a finite number of closest upper layer blocks. The deformation of the terrain can be, either because of the heightfield difference of the neighboring cells causing avalanches, or because of an applied vertical force causing land compression and displacement.

In the particle-based method, the deformable terrain (soil) can evolve and become unbound, thus, simulating soil behavior. Soil particles are generated when the applied horizontal force exceeds the shear impulse limit, thereby, updating the heightfield based on the volume of the generated soil particles. The particles have six degrees of freedom and are simulated using the multibody equations of motion. On reaching a dynamic equilibrium, the generated particles are merged back to the heightfield with a volume update [37].

When the tire begins to interact with the terrain, the contact forces between them are calculated at every iteration. These forces deform the terrain by compression and displacement or by soil particle generation as explained above and accordingly, an update is made on the terrain model shape. The new terrain shape is used in the next iteration in the calculation of the tire-soil contact forces. Therefore, there are continuous updates in the terrain shape based on the contact forces, which, in turn, are calculated based on the terrain shape updates. Before the tire-soil contact force calculation commences, the terrain is considered as a static soil grid. [38]

IV. CASE STUDY OF A TRACTOR MODEL

A tractor is considered as a case example in this study and is modeled using the semi-recursive multibody formulation

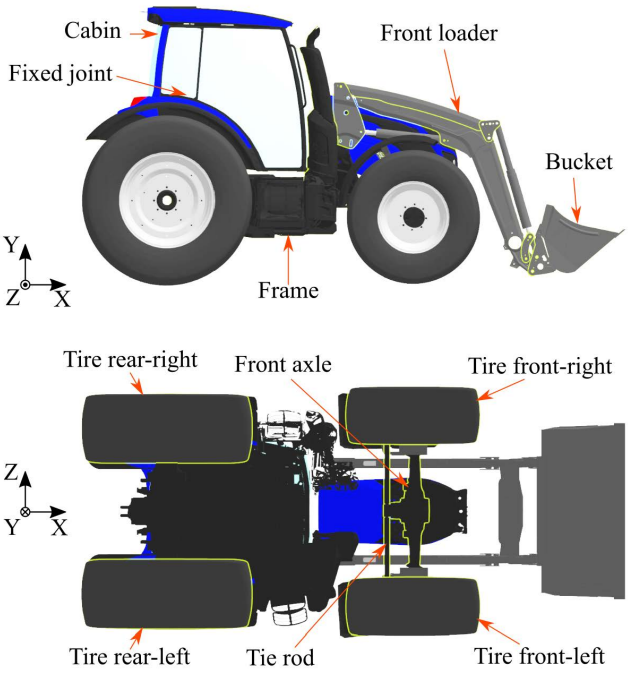

FIGURE 9. The multibody model of a tractor used in the case study [57].

explained in Sect. III-A. As shown in Fig. 9, the tractor model consists of 13 bodies, 15 joints, 28 joint coordinates, three cut-joints and 15 loop-closure constraints, and it has nine degrees of freedom. Tires are modeled using the lumped LuGre tire model explained in Sect. III-B. The deformable terrain is modeled as explained in Sect. III-C. The tractor simulation model is complex in nature and it utilizes small time-steps of 1.2 ms. It should be noted that the mechanical model of the tractor is inspired by the Valtra N174 model. The total weight of the tractor is 7833 kg, where 48.34% of the weight is in the front axle and 51.66% is on the rear axle and the wheelbase is 2.67 m. The tractor model is simulated in a C++ environment (compiler: Microsoft Visual Studio, version 14.1). For more details on the multibody modeling of the tractor, readers are referred to [57] and [38].

A. POWERTRAIN CONFIGURATIONS

A schematic of the topologies and transmissions of the four hybrid powertrain models developed in this study is shown in Fig. 10 and Fig. 11, respectively. The hybrid electric powertrain models have been simulated using MATLAB Simulink software. The selection of the powertrain models is based on the configurations used in commercial tractors and passenger vehicles. The series topology has been selected due to its classical nature and wide use in HEV while the series-parallel topology is selected due to the advantages it offers. Both topologies have been implemented in industrial tractors [58]. Benefits of series topologies equipped with CVT have been shown in [59]. The power-split configurations have been based on the Hybrid Synergy Drive systems used in Toyota passenger vehicles [60].

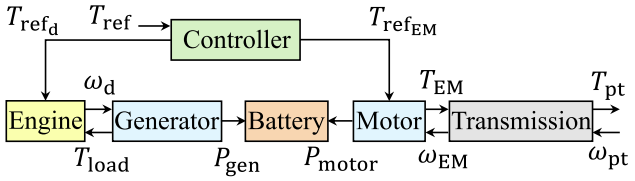

(a) Series topology used in the series AMT and series CVT configurations.

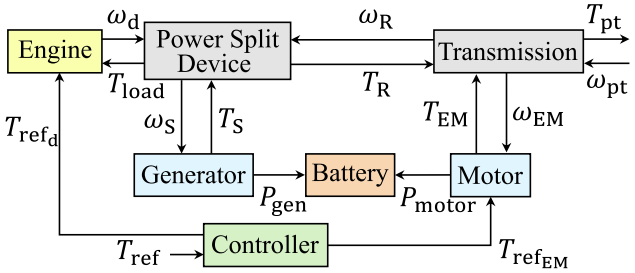

(b) Series-parallel topology used in the single PG and double PG configurations.

FIGURE 10. Schematic of the hybrid powertrain topologies.

The first model (series AMT) has a series topology (Fig. 10a) with an AMT as shown in Fig. 11a. The second model (series CVT) also has a series topology (Fig. 10a) with a CVT as shown in Fig. 11b. The third model (single PG) has a series-parallel topology (Fig. 10b) with a single planetary gear power-split device connected to the engine, transmission and generator, and a torque coupler merging the torque from the planetary gear ring and a CVT as shown in Fig. 11c. The fourth model (double PG) also has a series-parallel topology (Fig. 10b) with the planetary gear power-split device connected to a second planetary gear as shown in Fig. 11b. The series AMT model is considered as a benchmark for comparison purposes. All four models use same-sized diesel engine, electric machines (generator and motor) and battery models. The diesel engine power decided by the controller is used to determine the reference engine torque (T_{ref_d}). The reference torque for the motor ($T_{ref_{EM}}$) is determined by the controller based on T_{ref_d} and the torque requirement (T_{ref}). The specifications of the components used in the models are provided in Table 1.

B. CO-SIMULATION SETUP

The hybrid powertrain and the multibody tractor model are solved separately in a co-simulation platform developed in [61] (Fig. 12). The hybrid powertrain subsystem consists of the work cycle, controller, hybrid powertrain, and the communication manager. The work cycle provides the reference inputs required to drive the tractor, which include the reference torque demand (T_{ref}), reference velocity (v_{ref}), braking torque (T_{brake}), and the steering angle (θ_{steer}). The diesel engine, generator, battery, electric motor and transmission together comprise the hybrid powertrain. The hybrid powertrain subsystem is solved by the master simulation tool using a fixed-step discrete solver at a shorter time-step of 0.5 ms. Using this solver, the communication manager discretely handles data transfer between the subsystems through a TCP/IP socket connection at a time-step of 1.2 ms. The multibody

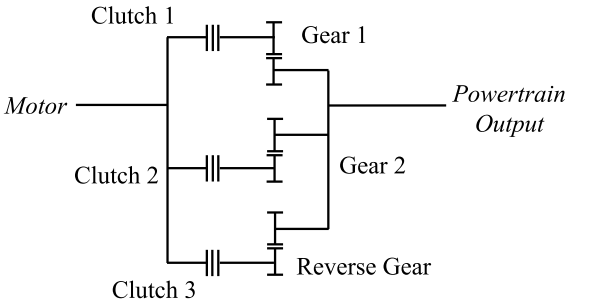

(a) Automated manual transmission (AMT) based gearbox used in the series AMT configuration.

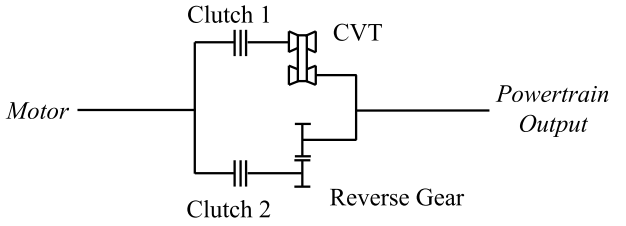

(b) Continuously variable transmission (CVT) based gearbox used in the series CVT configuration.

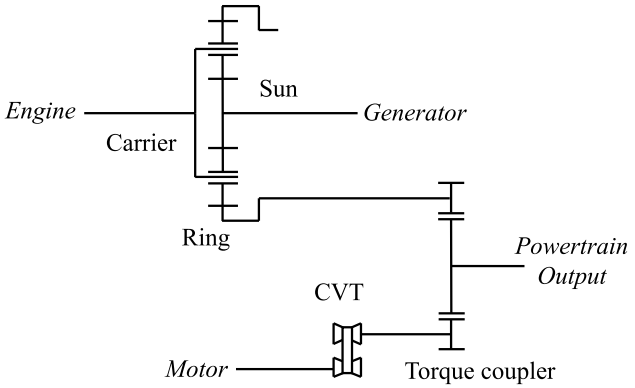

(c) Single planetary gear-based power-split device connected to the torque coupling transmission with CVT in the single PG configuration.

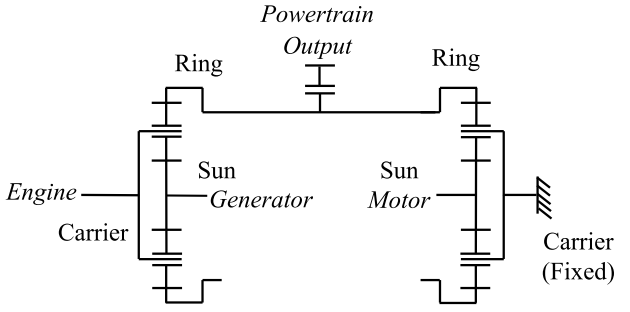

(d) Single planetary gear-based power-split device connected to a second planetary gear in the double PG configuration.

FIGURE 11. Schematics of the transmissions used in the four configurations.

tractor model is solved by a fourth order Runge-Kutta solver at a larger time-step of 1.2 ms as in [38] and [57]. These configurations allow the co-simulation to occur at a low computational cost with real-time capability. For every time-step of the multibody dynamics sub-simulation, the T_{pt}, T_{brake}, and θ_{steer} are sent from the powertrain sub-simulation to the

TABLE 1. Specifications of the components used in the models.

Component	Parameter	Value
Engine	Maximum power (kW)	157
	Maximum torque (Nm)	900
	Maximum speed (rpm)	2300
Motor	Nominal power (kW)	264
	Nominal torque (Nm)	720
	Nominal speed (rpm)	3500
Generator	Nominal power (kW)	141
	Nominal torque (Nm)	900
	Nominal speed (rpm)	1500
Battery	Nominal power (kW)	158
	Nominal battery voltage (V)	792
	Nominal battery capacity (kWh)	15
AMT	Gear 1 ratio	1.5
	Gear 2 ratio	1.3
	Reverse gear	4
CVT	Maximum gear ratio	7
	Minimum gear ratio	1.2
	Reverse gear	2
Planetary gear	Ring-sun gear ratio	2.53
	Sun-planet gear ratio	1.31

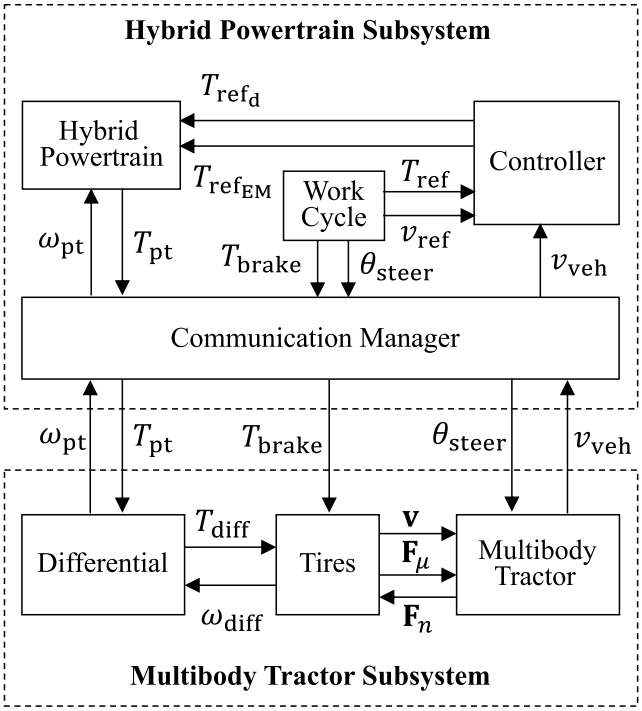

FIGURE 12. Co-simulation setup between multibody tractor subsystem and hybrid powertrain subsystem.

multibody sub-simulation while the velocity of the tractor (v_{veh}) and ω_{pt} are sent back to the powertrain sub-simulation.

C. WORK CYCLE

The DLG-Powermix consists of 14 individual cycles describing the loads on a tractor while performing typical tasks or combinations of tasks like cultivating, ploughing, mowing, and spreading manure or transportation [39]. These cycles are used to measure the tractor's output, fuel consumption and energy-efficiency. In this study, a single ploughing cycle (Z2P) has been selected from the 14 DLG-Powermix cycles to conduct the simulations in a virtual environment shown in Fig. 13.

The tractor begins from the initial position with an uphill drive, continuing in a circular trajectory to complete the lap with a downhill maneuver. In the 960-second duration of the cycle, the tractor drives 14.5 laps in the circular path described. The tractor maintains an average speed of 8 km/h, which is the reference speed of the Z2P cycle of the DLG-Powermix. The ploughing scenario is replicated by applying a pulling force at the back of the tractor the value for which is taken from a look-up table containing the DLG-Z2P data (Fig. 14). The inclination angle of the tractor cabin is also shown in Fig. 14 to indicate the slope of the path travelled. The multibody system outputs in each lap are not identical due to the deformable terrain. The outputs of the four models also vary slightly due to the chaotic nature of the soil particles. However, the differences are minor and within an acceptable range.

V. RESULTS AND DISCUSSION

This section presents results of the ploughing work cycle of the DLG-Powermix for the series AMT, series CVT, single PG and double PG powertrain models combined with the multibody tractor on the deformable terrain. The fuel consumption, diesel engine power, battery *SOC* and electric motor power are shown in Fig. 15. The electric motor energy consumption and recovery, and the diesel engine energy consumption are shown in Fig. 16. The electric motor efficiency and energy loss are shown in Fig. 17. The integration time is shown in Fig. 18.

A. FUEL CONSUMPTION, DIESEL ENGINE POWER, BATTERY SOC AND ELECTRIC MOTOR POWER

It can be observed from Fig. 15 that the fuel consumption of the four models steadily increases during the simulation. For each topology studied, the fuel consumption is almost the same as noted in Table 2. However, the series parallel topology brings a marginal improvement in fuel consumption, with the single PG consuming 4.1% lower fuel than the benchmark series AMT. Compared to a conventional tractor with same sized diesel engine the benchmark series AMT attains fuel savings of 30.7% which shows the benefits of hybridization. Such fuel savings of hybrid architectures with respect to conventional tractors are consistent with the values obtained in literature such as in [21], [23], and [31]. However, it is to be noted that the developed simulation toolset does not aim to produce exact values of fuel and energy consumption, which would require experimental validation of each studied configuration. The presented method only aims to provide a relative comparison between various hybrid architectures.

The three modes of the control strategy (Fig. 7) can be distinguished from the diesel power plot in Fig. 15. In the

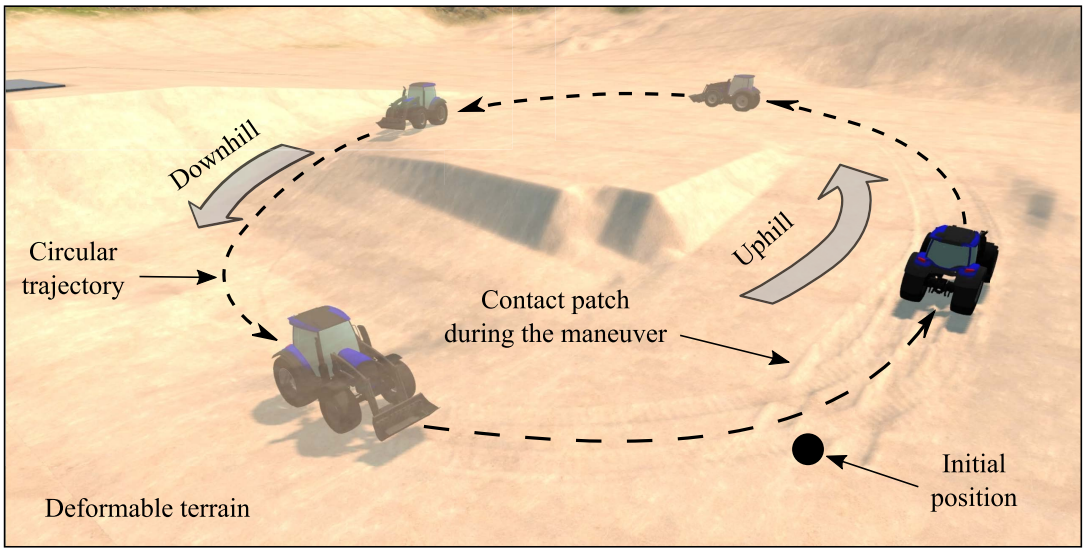

FIGURE 13. Trajectory of the tractor on the deformable terrain in the virtual simulation environment.

beginning of the work cycle the battery mode can be observed where diesel power is at its minimum level (P_{d_min}). Here, the fuel consumption is seen to increase at a low rate during this mode since the diesel power is low. The max mode is observed next, when the engine power rises gradually trying to attain the same value as the motor power (P_{load}) in accordance with the control strategy. As a result, the fuel consumption rises more steeply. It is followed by the hybrid mode when the engine provides a constant optimal power value (P_{d_opt}). As dictated by the controller, only the hybrid and max modes are observed during the remaining duration of the work cycle because the *SOC* remains below its upper limit. Therefore, the fuel consumption increases at a corresponding rate.

The mode change pattern observed in the diesel power plot is dependent on the battery *SOC* and electric motor power. The battery *SOC* starts to decline at the beginning of the work cycle. When the motor power is low the depletion of battery *SOC* occurs at a low rate. At the same time, the diesel power replenishes the battery charge through the generator. When the motor power peaks, steeper declines in battery *SOC* can be observed. The *SOC* of each topology appears to follow similar patterns. The *SOC* of the power-split models, however, are consistently higher than that of the series models. The double PG model achieves the highest final *SOC* level among the four models.

The motor power behaviour of the four models reflect the traction demand which is primarily fulfilled by the electric motor in the studied configurations. The traction demand is influenced by the pulling force as well as the inclination shown in Fig. 14. Each downhill maneuver is demarcated by low motor power values indicating regenerative braking occurring in those instances. When there is either an uphill maneuver or a high value of pulling force acting, then the motor power is observed to increase due to the higher traction demand. The motor power peaks when the traction demand is the highest as a result of the combined effect of the pulling power and uphill maneuver. In the entire duration of the work cycle, the motor power of the power-split models are relatively lower compared to the series models because the diesel power partially assists the motor in fulfilling the traction demand. These lower values of the motor power result in lower depletion of battery charge as seen by the higher battery *SOC* values of the single PG and double PG models.

The results shown in Fig. 15 indicate that the diesel engine performs in a similar manner resulting in minor differences in diesel power and fuel consumption. This is expected since the same control strategy has been used for different topologies. However, the advantage of the power-split topology is clearly seen in the motor power and battery *SOC* where the traction load is shared between the diesel engine and the electric motor. Having a mechanical connection between the engine and the transmission also eliminates losses due to double energy conversions. The surplus battery charge in the power-split models compared to the series models can be used to introduce an electric mode where the engine can be turned off to increase fuel savings. Therefore, a need for topology-specific control strategies can be identified from the results in Fig. 15 such that the defined rules complement the topology, thereby increasing fuel-savings.

The final *SOC* levels achieved by all four models are within the acceptable range seen in similar works [9], [16], [62], [63]. However, the double PG model emerges as the superior configuration due to the higher final *SOC* achieved. Based on fuel savings, both the single PG and double PG show advantages compared to the series models. The results achieved in this study are consistent with the fuel savings achieved in [9], [16], and [23] through improved configurations, transmissions, and controllers. However, the powertrain configurations presented for a multibody tractor model in this study have not been evaluated in other works.

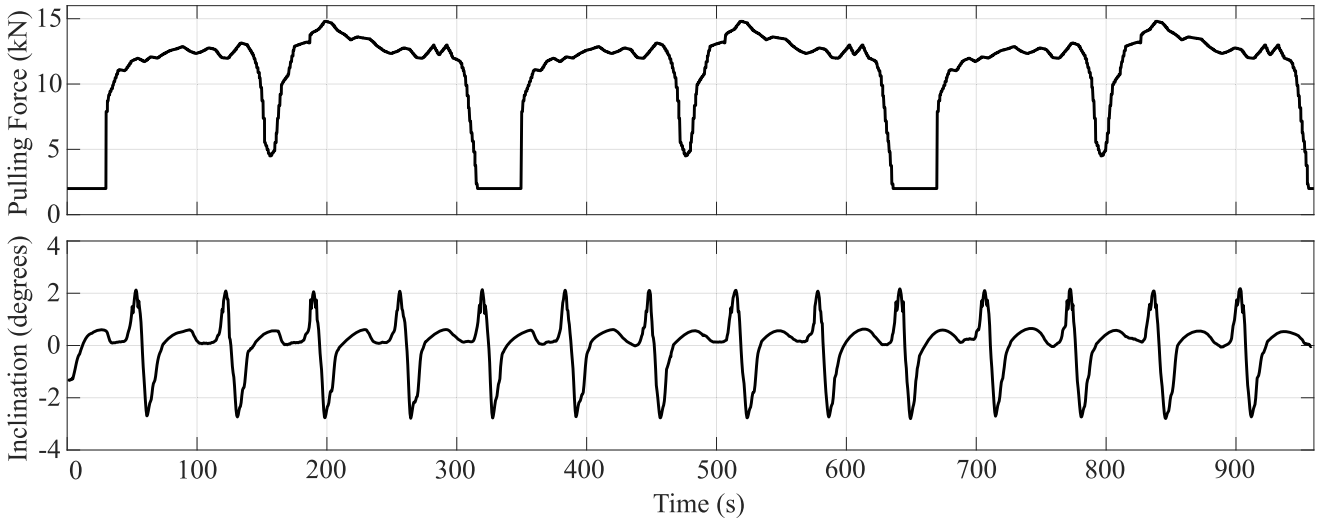

FIGURE 14. Pulling force profile of the Z2P work cycle of the DLG-Powermix and inclination of the tractor in the virtual simulation environment.

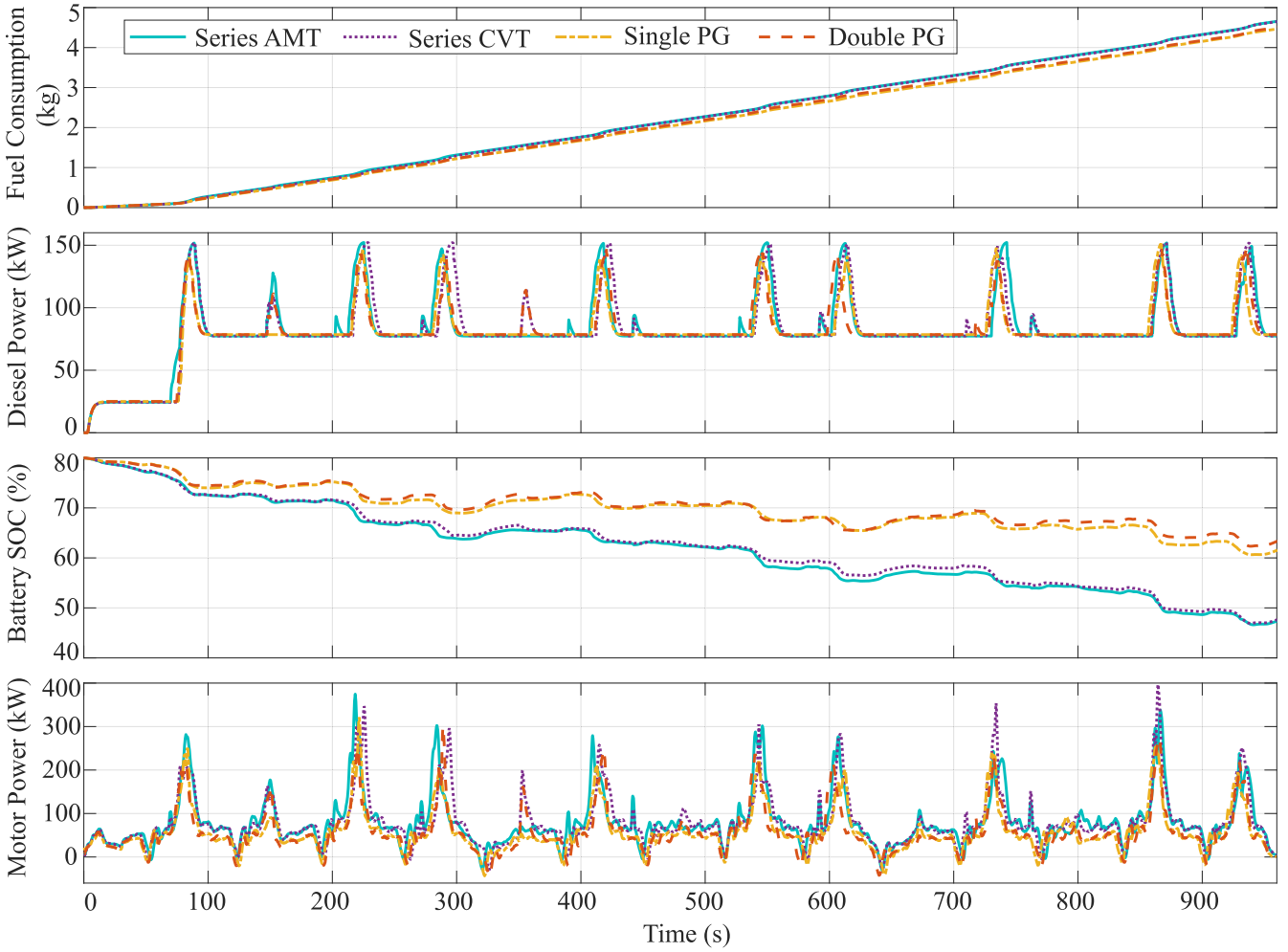

FIGURE 15. Fuel consumption, diesel engine power, battery *SOC* and electric motor power results.

B. ENERGY CONSUMPTION AND RECOVERY

The total energy consumption of each configuration has been calculated as the sum of the fuel energy consumed by the diesel engine and the energy consumed by the electric drive motor. This takes into account all the energy conversions starting from the fuel energy used to charge the battery as well as to provide traction demand in the power-split architectures, and the energy depleted from the battery due to the

TABLE 2. Comparison of total energy consumption, motor energy recovery, and fuel economy.

	Series AMT (benchmark)	Series CVT	Single PG	Double PG	Improvement in Series CVT	Improvement in Single PG	Improvement in Double PG
Fuel Consumption	4.66 kg	4.65 kg	4.47 kg	4.51 kg	0.2%	4.1%	3.2%
Total Energy Consumption	271.04 MJ	270.86 MJ	244.78 MJ	246.15 MJ	0.1%	9.7%	9.2%
Motor Energy Recovery	339.36 kJ	347.53 kJ	981.96 kJ	1062.29 kJ	2.4%	189.4%	213.0%
Motor Energy Loss	5.16 MJ	4.48 MJ	2.68 MJ	2.45 MJ	13.2%	48.1%	52.5%
Average Motor Efficiency	92.3%	92.9%	98.8%	94.1%	0.6%	6.6%	1.8%

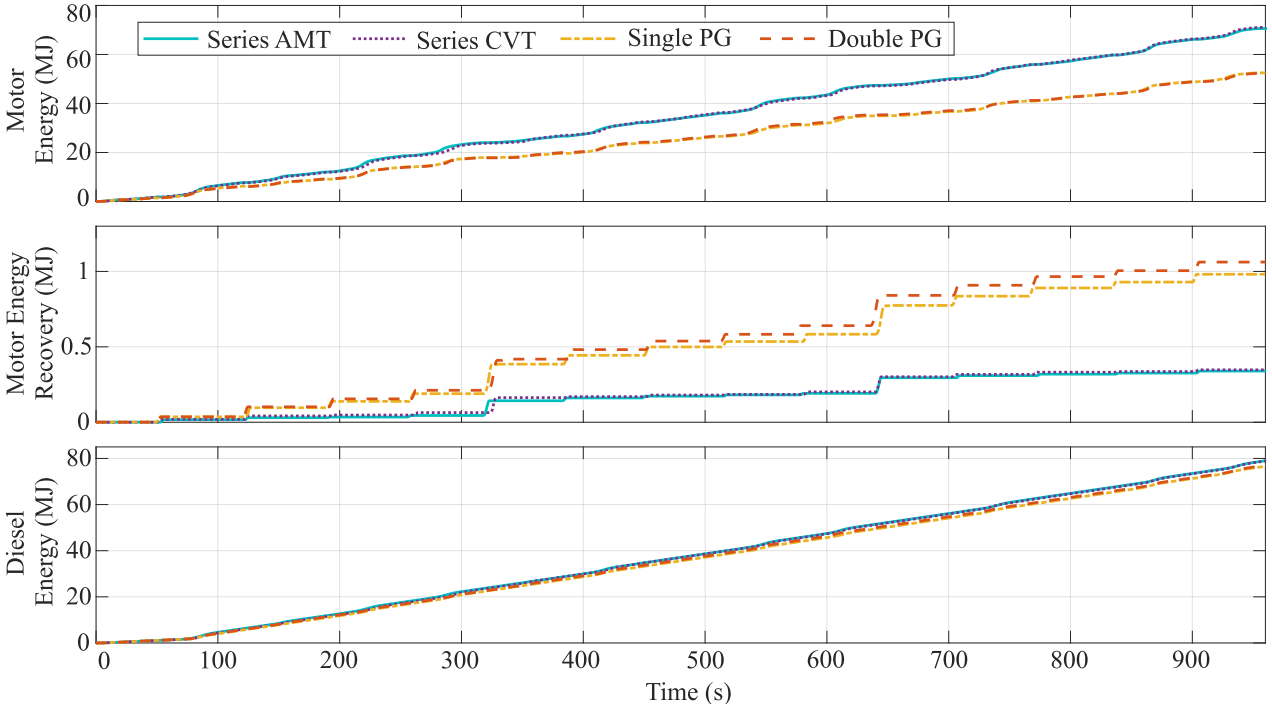

FIGURE 16. Electric motor energy consumption, electric motor energy recovery and diesel engine energy consumption results.

energy consumed by the drive motor to provide the traction demand.

The series AMT and the series CVT models consume higher electric motor energy, as seen in Fig. 16, since the electric motor power of these models, shown in Fig. 15, is also relatively higher than that of the power-split models. This is because the motor alone fulfills the entire traction demand. In case of the power-split models, the motor energy consumption is observed to be lower in Fig. 16. This is because the diesel engine is connected to the transmission through the power-split device and supports the motor in fulfilling the traction demand. The motor energy increases more steeply at every uphill maneuver accompanied by high pulling force because of the corresponding peak in motor power.

Motor energy recovery is observed to occur during the downhill maneuvers as the motor power becomes negative. The overall energy recovery in the simulated work cycle is low compared to the energy consumption. This is because the work cycle has a constant average speed, allowing energy recovery to occur only briefly during the downhill maneuvers. However, among the four models, the series AMT and series CVT recover the lowest amount of energy, while the power-split models recover the most energy. The higher recovery comes from the diesel engine power constantly delivered to the ring gear of the power-split device, which becomes a surplus during downhill maneuvers and is recovered by the electric motor.

All four models have similar values of diesel engine energy consumption, which is also reflected in the fuel consumption and diesel power plots since the controller regulates the diesel power in a similar manner for all four models. There is a reduction of 9.7% and 9.2% in the total energy consumed

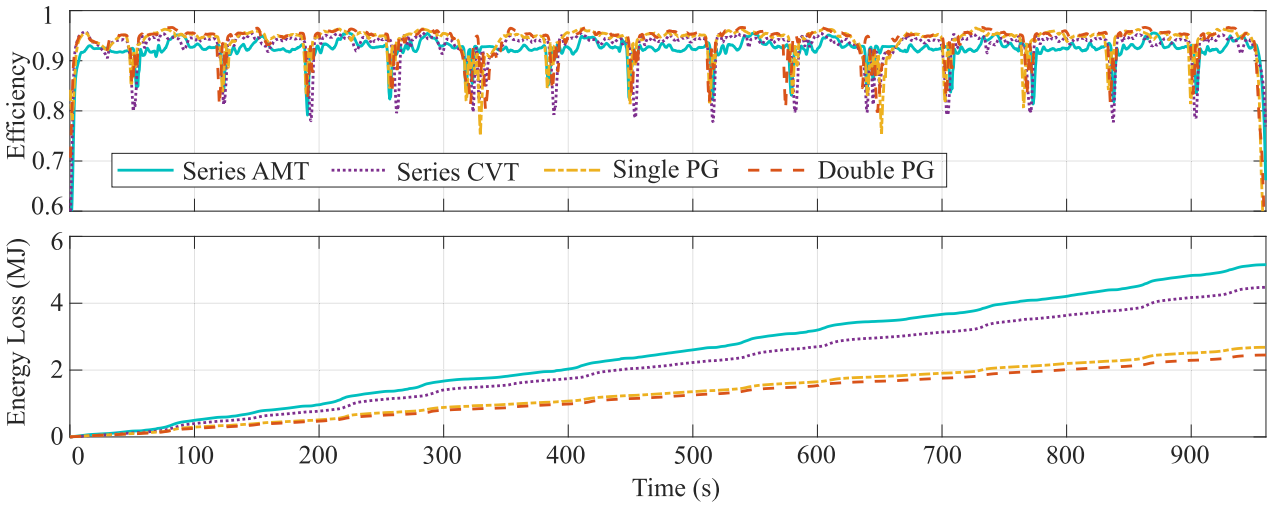

FIGURE 17. Efficiency and energy loss results of the electric motor.

in the single PG and double PG models, respectively, compared to the series AMT, as noted in Table 2. Compared to a conventional tractor with same sized diesel engine the benchmark series AMT consumed 6.3% lower total energy. This indicates the potential of energy savings by hybridization which reduces the high fuel energy losses incurred by running the tractor solely using a diesel engine. Higher motor energy recoveries of 189.4% and 213.0% are achieved by the single PG and double PG models, respectively, compared to the series AMT. The improvement achieved by the models substantiates the advantage of the power-split configuration in the studied case. It also further highlights the need for topology-specific controller that can reduce the unnecessary surplus power delivered by the diesel engine at the ring gear of the power-split device.

C. ELECTRIC MOTOR EFFICIENCY AND ENERGY LOSS

The electric motor efficiency, which is obtained from the motor efficiency map (Fig. 3a) corresponding to the torque and speed of the motor, is shown in Fig. 17. The obtained efficiency is used to calculate the motor power loss using Eqs. (3), (4) and (5) as the difference between the input (P_{motor}) and output (P_{load}) power of the motor. The motor efficiency of the AMT model is observed to be the lowest among the four models in Fig. 17. Even though the series CVT model also has a series topology, it achieves higher motor efficiencies by selecting speed ratios that allow the motor to avoid the low efficiency regions in the efficiency map. At the instances when low motor power is observed in Fig. 15, the efficiencies of all four models are seen to drop because at low torques and speeds the efficiency of the electric motor is low.

The electric motor energy losses for the AMT and CVT models, shown in Fig. 17, follow similar patterns as the motor energy consumption (Fig. 16). This is because when higher amount of energy consumption leads to higher losses and vice versa. However, throughout the cycle, the series CVT model maintains higher motor efficiency compared to the series AMT by regulating the speed ratio. Consequently, the series CVT model incurs 13.2% lower energy loss compared to the AMT model while consuming the same amount of total energy. The average electric motor efficiency is 0.6% higher in the series CVT compared to the the series AMT, as noted in Table 2. The higher motor efficiency and lower motor energy loss exhibited in the CVT model shows the upside of having controllable speed ratios in a hybrid powertrain.

Motor energy losses are lower in the power-split models compared to the series models due to the overall lower consumption of motor energy. The single PG configuration includes a CVT which keeps the motor efficiency higher than all the other models with a 6.6% improvement compared to the series AMT. However, the higher efficiency regions of the electric motor correspond to higher torques and speeds resulting in higher motor power consumption for the single PG model. Therefore, the single PG attains a much higher average motor efficiency but consumes higher motor energy compared to the double PG model in the process. As a result, the motor energy losses are lower for the double PG compared to the single PG due to lower motor energy consumption.

D. REAL-TIME CAPABILITY OF THE SYSTEM

Figure 18 shows the integration time for all the four models along with the time-step of the multibody tractor simulation. The integration times of the four models are observed to fluctuate in the range of 0.7 ms to 1.1 ms, while the time-step of the tractor simulation is 1.2 ms. As depicted in Fig. 18, the integration times of all the four models are always less than the time-step. Therefore, it can be said that the hybrid electric tractor simulation models developed in this study are real-time capable. Their computation is synchronized to real-time, such that a human operator can use these models to simulate specific work cycles.

Among the four models, the series AMT and double PG achieve the lowest integration time while the series CVT and single PG have relatively higher integration time. The higher computation time taken by these two models is due

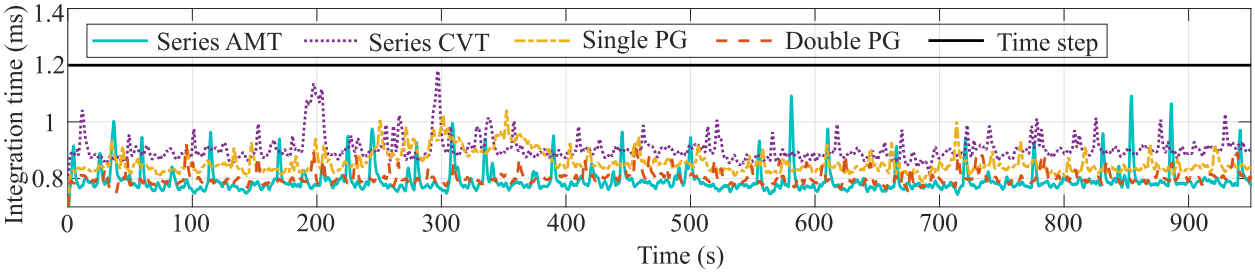

FIGURE 18. Integration time for the simulations.

to the addition of the CVT speed ratio controller which adds complexity to these models compared to the others. However, even with the added complexity these models appear to be real-time capable. The series AMT, being the computationally simpler model among the four, emerges as the most numerically efficient one. The high numerical efficiency achieved by all four models allows room to add more complexity to the model during future development while preserving the real-time capability.

E. DISCUSSION

The simulation of the multibody tractor in the three-dimensional virtual environment shown in Fig. 13 exhibits the utility of the real-time capable model in simulating standard as well as user-specific work cycles. In contrast to passenger vehicles, NRMM are driven off-road in various kinds of terrain and perform various functions different from transportation. The models studied in this work account for the three-dimensional dynamics of a complex NRMM on undulating terrain of varying gradient in the comparative energy analysis of four different powertrain architectures. The effects of these dynamical factors are incorporated in the energy consumption results shown in this work and are highly relevant to NRMM.

The Z2P ploughing cycle of the DLG-Powermix has been utilized to demonstrate the capability of the model to simulate standardized work cycles of NRMM in machine-specific scenarios. The three-dimensional maneuver performed by the tractor while the pulling force profile of the DLG-Z2P is applied to it shows how a human operator can simulate and investigate powertrain efficiencies using the developed models. The capability to simulate customized work cycles through human operators in real-time is significant to NRMM because the work cycles for such machinery is often unknown prior to operation. While the work cycle simulated in this study includes only traction loads from a ploughing scenario, NRMM working operations include other complicated scenarios like excavation, compaction, bucket loading and cultivation. The presented model can be developed further to model the dynamic loading conditions of such scenarios. For example, a soil digging and dumping scenario using a hydraulically actuated front loader of the tractor has been investigated in [64].

Accessible data like efficiency maps have been utilized in the component models, making it easy to change component sizing and other characteristics. The co-simulation setup described in this study combined the system-level powertrain simulation with the detailed multibody tractor model, thereby achieving real-time performance with sufficient accuracy to conduct energy-efficiency analysis. Therefore, the model complexity required in NRMM simulation was maintained along with the ability of the model to compare various hybrid electric powertrain configurations essential in the hybridization of NRMM.

Existing literature, on one hand, encompasses comparisons of powertrain architectures using simplistic vehicle models, and, on the other hand, includes detailed physics-based vehicle models studying limited hybrid electric powertrain configurations. This study has combined the detailed multibody tractor model with various powertrain models which allows comparative energy efficiency analyses with the benefits of detailed physics-based NRMM models. Although simpler longitudinal models have been widely used in powertrain comparisons in existing literature, the multibody real-time co-simulation models presented in this study have captured the dynamical aspects important to NRMM in a real-time framework that can be utilized by human operators.

When considering the hybridization of a NRMM powertrain there are several factors to consider, like fuel savings, component sizing, manufacturability, energy management systems and cost. This study demonstrated the possible improvements from selection of powertrain architecture through relative comparison. Further improvements can be investigated by developing the model to replicate the tire-soil interaction of the case application accurately along with model validation to achieve exact values of fuel and energy consumption. The sizing of the components can be improved according to the requirements of the selected topology. When the driving cycle is known and fixed, global optimal solution can be used to define the rules of the supervisory control. Advanced real-time control strategies like model predictive control can also be implemented on the developed model and investigated for improvements in energy management.

VI. CONCLUSION

This study described the development of four hybrid electric powertrain models within the framework of real-time multibody simulation and compared their energy efficiency and real-time capability. The series AMT model has a series topology using an AMT, and serves as a benchmark model

in this study. The series CVT model has a series topology using a CVT as the forward gear. The single PG model has a series-parallel topology using a single planetary gear-based power-split device, and a CVT and torque coupler in the transmission. The double PG model also has a series-parallel topology using a single planetary gear-based power-split device and, in contrast to the single PG, a second planetary gear in the transmission. The case example of a tractor modeled using semi-recursive multibody formulation was co-simulated with the four powertrains and tested in a virtual simulation environment under the loading conditions of the DLG-powermix ploughing work cycle. The fuel consumption, diesel engine power, battery state of charge, electric motor power, energy consumption and recovery, electric motor efficiency, electric motor energy losses, and integration time of the four models were analyzed.

The comparative analysis showed that all the four models showed similar fuel consumption due to the same rule-based supervisory control of the engine power. However, the two studied power-split models achieved improvements 9.7% and 9.2% in total energy consumption compared to the series AMT model by sharing the high traction demand of the work cycle between the diesel engine and the electric motor. The power-split models also recovered significantly higher energy from the electric motor and incurred lower motor energy losses. Such improvements indicate the suitability of the power-split configuration over the series configuration in the simulated case study. Among the power-split configurations, the double PG model achieved highest motor energy recovery and lowest motor energy losses. All four models were seen to be real-time capable with short integration time allowing the possibility of adding more complexity to the model during future development of this work.

The accuracy of the results presented in this study have not been validated by actual measurements due to the lack of experimental data. However, the energy and fuel consumption of the models show good agreement with simulation results and experimental data found in existing literature. Although NRMM have varying performance characteristics, the traction and peak power requirements seen in this study are reasonable and, the diesel engine, electric machines and battery behave in a logical manner. The developed simulation toolset is meant for relative comparison between hybrid architectures and does not claim to generate the realistic absolute values of fuel and energy consumption. This toolset can be used by manufacturers in the selection of powertrain configurations based on their relative performances in metrics like fuel consumption, energy consumption and energy recovery.

The developed model demonstrated the capability to evaluate the energy efficiency of powertrain concepts in the framework of real-time multibody simulations that allow human operators to simulate standard as well as non-standard work cycles. The improvements brought about by selection of topology and transmission have been illustrated in the results of this study. Other areas of improvement of powertrain like component sizing and control optimization can also be investigated using the developed model. Small percentage improvements achieved in the simulated case study can also indicate high values of total energy and fuel savings due to the extended duration of the work cycles in real-life NRMM applications. Such improvements can be effectively investigated using computer simulation models such as the one developed in this work.

In future works, the energy consumption characteristics presented in this work can be validated. This study can be extended to develop contact models of the transmission components to take into account the time-varying mechanical power losses in the system. Emission studies can be performed to explore the possible reductions in NRMM emissions as a result of hybridization. The hydraulically actuated front loader of the tractor can be connected to the hybrid electric powertrains to observe the actuator forces and the effects of the power drawn by them on the diesel engine and battery in a soil digging work cycle. The effect of hybrid electric powertrain parameters on the vehicle performance can be studied. Driving styles of various operators and their effect on energy efficiency can be studied using the developed models. Furthermore, the multibody approach used in this study allows further development in the tire-soil interaction to replicate agricultural soil behavior, gamification [47], to aid operator training and the development of a heads-up display [57] to show real-time hybrid powertrain information to the driver.

REFERENCES

[1] IEA. (2021). *Global Electric Vehicles Outlook 2021*. [Online]. Available: https://iea.blob.core.windows.net/assets/ed5f4484-f556-4110-8c5c-4ede8bcba637/GlobalEVOutlook2021.pdf

[2] R. Yuan, T. Fletcher, A. Ahmedov, N. Kalantzis, A. Pezouvanis, N. Dutta, A. Watson, and K. Ebrahimi, "Modelling and co-simulation of hybrid vehicles: A thermal management perspective," *Appl. Thermal Eng.*, vol. 180, Nov. 2020, Art. no. 115883.

[3] L. Fang, R. Zhang, C. Vanden Heuvel, R. Serban, and D. Negrut, "Chrono: GPU: An open-source simulation package for granular dynamics using the discrete element method," *Processes*, vol. 9, no. 10, p. 1813, Oct. 2021.

[4] D. Negrut, R. Serban, A. Elmquist, D. Hatch, E. Nutt, and P. Sheets, "Autonomous vehicles in the cyberspace: Accelerating testing via computer simulation," SAE Tech. Paper 01-1078, 2018.

[5] J.-S. Chen, "Energy efficiency comparison between hydraulic hybrid and hybrid electric vehicles," *Energies*, vol. 8, no. 6, pp. 4697–4723, May 2015.

[6] B. Suh, A. Frank, Y. J. Chung, E. Y. Lee, Y. H. Chang, and S. B. Han, "Powertrain system optimization for a heavy-duty hybrid electric bus," *Int. J. Automot. Technol.*, vol. 12, no. 1, pp. 131–139, Feb. 2011.

[7] N. Muralidhar, M. Himabindu, and R. V. Ravikrishna, "Modeling of a hybrid electric heavy duty vehicle to assess energy recovery using a thermoelectric generator," *Energy*, vol. 148, pp. 1046–1059, Apr. 2018.

[8] M. Esfahanian, A. Safaei, H. Nehzati, V. Esfahanian, and M. M. Tehrani, "MATLAB-based modeling, simulation and design package for eletric, hydraulic and flywheel hybrid powertrains of a city bus," *Int. J. Automot. Technol.*, vol. 15, no. 6, pp. 1001–1013, Oct. 2014.

[9] B. Mashadi and S. A. M. Emadi, "Dual-mode power-split transmission for hybrid electric vehicles," *IEEE Trans. Veh. Technol.*, vol. 59, no. 7, pp. 3223–3232, Sep. 2010.

[10] H. Guo, Q. Sun, C. Wang, Q. Wang, and S. Lu, "A systematic design and optimization method of transmission system and power management for a plug-in hybrid electric vehicle," *Energy*, vol. 148, pp. 1006–1017, Apr. 2018.

[11] T. Hofman, S. Ebbesen, and L. Guzzella, "Topology optimization for hybrid electric vehicles with automated transmissions," *IEEE Trans. Veh. Technol.*, vol. 61, no. 6, pp. 2442–2451, Jul. 2012.

[12] S. Di Cairano, W. Liang, I. V. Kolmanovsky, M. L. Kuang, and A. M. Phillips, "Power smoothing energy management and its application to a series hybrid powertrain," *IEEE Trans. Control Syst. Technol.*, vol. 21, no. 6, pp. 2091–2103, Nov. 2012.

[13] C. Qi, Y. Zhu, C. Song, G. Yan, F. Xiao, X. Zhang, J. Cao, and S. Song, "Hierarchical reinforcement learning based energy management strategy for hybrid electric vehicle," *Energy*, vol. 238, Jan. 2022, Art. no. 121703.

[14] L. Li, S. Coskun, F. Zhang, R. Langari, and J. Xi, "Energy management of hybrid electric vehicle using vehicle lateral dynamic in velocity prediction," *IEEE Trans. Veh. Technol.*, vol. 68, no. 4, pp. 3279–3293, Apr. 2019.

[15] Y. Li, H. He, J. Peng, and H. Wang, "Deep reinforcement learning-based energy management for a series hybrid electric vehicle enabled by history cumulative trip information," *IEEE Trans. Veh. Technol.*, vol. 68, no. 8, pp. 7416–7430, Aug. 2019.

[16] S.-Y. Chen, C.-H. Wu, Y.-H. Hung, and C.-T. Chung, "Optimal strategies of energy management integrated with transmission control for a hybrid electric vehicle using dynamic particle swarm optimization," *Energy*, vol. 160, pp. 154–170, Oct. 2018.

[17] M. G. Tehrani, J. Kelkka, J. Sopanen, A. Mikkola, and K. Kerkkanen, "Electric vehicle energy consumption simulation by modeling the efficiency of driveline components," *SAE Int. J. Commercial Vehicles*, vol. 9, no. 1, pp. 31–40, 2016.

[18] K. Tammi, T. Minav, and J. Kortelainen, "Thirty years of electro-hybrid powertrain simulation," *IEEE Access*, vol. 6, pp. 35250–35259, 2018.

[19] J. Wang, Z. Yang, S. Liu, Q. Zhang, and Y. Han, "A comprehensive overview of hybrid construction machinery," in *Proc. Adv. Mech. Eng.*, vol. 8, no. 3, 2016, Art. no. 1687814016636809.

[20] A. Lajunen, P. Sainio, L. Laurila, J. Pippuri-Mäkeläinen, and K. Tammi, "Overview of powertrain electrification and future scenarios for non-road mobile machinery," *Energies*, vol. 11, no. 5, p. 1184, 2018.

[21] A. Lajunen, "Energy efficiency of conventional, hybrid electric, and fuel cell hybrid powertrains in heavy machinery," SAE Tech. Paper 2015-01-2829, 2015.

[22] F. Mocera, V. Martini, and A. Somà, "Comparative analysis of hybrid electric architectures for specialized agricultural tractors," *Energies*, vol. 15, no. 5, p. 1944, Mar. 2022.

[23] V. Randive, S. C. Subramanian, and A. Thondiyath, "Design and analysis of a hybrid electric powertrain for military tracked vehicles," *Energy*, vol. 229, Aug. 2021, Art. no. 120768.

[24] T.-S. Kwon, S.-W. Lee, S.-K. Sul, C.-G. Park, N.-I. Kim, B.-I. Kang, and M.-S. Hong, "Power control algorithm for hybrid excavator with supercapacitor," *IEEE Trans. Ind. Appl.*, vol. 46, no. 4, pp. 1447–1455, Jul. 2010.

[25] Z. Qin, Y. Luo, K. Li, and H. Peng, "Optimal design of a novel hybrid electric powertrain for tracked vehicles," *Energies*, vol. 10, no. 12, p. 2141, Dec. 2017.

[26] M. A. Bastin and R. P. Jones, "Development of a multibody systems model for investigation of the effects of hybrid electric vehicle powertrains on vehicle dynamics," *Int. J. Online Eng.*, vol. 11, no. 6, pp. 33–37, 2015.

[27] H. de Carvalho Pinheiro, A. Messana, L. Sisca, A. Ferraris, A. G. Airale, and M. Carello, "Torque vectoring in electric vehicles with in-wheel motors," in *IFToMM World Congress on Mechanism and Machine Science*, vol. 73. Cham, Switzerland: Springer, 2019, pp. 3127–3136.

[28] B. Xu, C. Xiang, Y. Qin, P. Ding, and M. Dong, "Semi-active vibration control for in-wheel switched reluctance motor driven electric vehicle with dynamic vibration absorbing structures: Concept and validation," *IEEE Access*, vol. 6, pp. 60274–60285, 2018.

[29] D. Liu, J. Zhang, D. Zhang, G. Liu, and H. Yu, "Experimental and numerical analysis of the seat track vibrations caused by engine starts in a power-split hybrid electric vehicle," *Proc. Inst. Mech. Eng. D, J. Automobile Eng.*, vol. 231, no. 3, pp. 395–404, Feb. 2017.

[30] E. Baharudin, J. Nokka, H. Montonen, P. Immonen, A. Rouvinen, L. Laurila, T. Lindh, A. Mikkola, J. Sopanen, and J. Pyrhönen, "Simulation environment for the real-time dynamic analysis of hybrid mobile machines," in *Proc. 11th Int. Conf. Multibody Syst., Nonlinear Dyn., Control*, vol. 6, Aug. 2015, Art. no. V006T10A073.

[31] J. Nokka, L. Laurila, and J. Pyrhönen, "Virtual simulation in energy efficient hybrid powertrain design," in *Proc. 16th Eur. Conf. Power Electron. Appl.*, Aug. 2014, pp. 1–12.

[32] J. G. D. Jalon and E. Bayo, *Kinematic and Dynamic Simulation of Multibody Systems: The Real-Time Challenge*. New York, NY, USA: Springer-Verlag, 1994.

[33] C. C. D. Wit, R. Horowitz, and P. Tsiotras, *New Directions in Nonlinear Observer Design*. London, U.K.: Springer, 1999.

[34] C. Canudas de Wit and P. Tsiotras, "Dynamic tire friction models for vehicle traction control," in *Proc. 38th IEEE Conf. Decis. Control*, Jun. 1999, pp. 3746–3751.

[35] M. Pla-Castells, I. Garcia, and R. J. Martinez, "Approximation of continuous media models for granular systems using cellular automata," in *Proc. 6th Int. Conf. Cellular Automata Res. Ind.*, Amsterdam, The Netherlands, 2004, pp. 230–237.

[36] M. Pla-Castells, I. Garcia-Fernandez, and R. J. Martinez, "Interactive terrain simulation and force distribution models in sand piles," in *Proc. 7th Int. Conf. Cellular Automata Res. Ind.*, Perpignan, France, 2006, pp. 392–401.

[37] D. Holz, T. Beer, and T. Kuhle, "Soil deformation models for real-time simulation: A hybrid approach," in *Proc. 6th Workshop Virtual Reality Interact. Phys. Simulations*, Karlsruhe, Germany, 2009, pp. 21–30.

[38] S. Jaiswal, P. Korkealaakso, R. Åman, J. Sopanen, and A. Mikkola, "Deformable terrain model for the real-time multibody simulation of a tractor with a hydraulically driven front-loader," *IEEE Access*, vol. 7, pp. 172694–172708, 2019.

[39] C. Pieke, W. Stark, F. Pfister, and C. Schyr, "DLG powermix on the dynamometer," *ATZoffhighway Worldwide*, vol. 10, no. 2, pp. 26–31, Jun. 2017.

[40] M. F. M. Sabri, K. A. Danapalasingam, and M. F. Rahmat, "A review on hybrid electric vehicles architecture and energy management strategies," *Renew. Sustain. Energy Rev.*, vol. 53, pp. 1433–1442, Jan. 2016.

[41] J. B. Heywood, *Internal Combustion Engine Fundamentals*. New York, NY, USA: McGraw-Hill, 1988.

[42] P. Immonen, "Energy efficiency of a diesel-electric mobile working machine," Ph.D. dissertation, Dept. Elect. Eng., Lappeenranta Univ. Technol., Lappeenranta, Finland, 2013.

[43] M. Laurén, G. Goswami, A. Tupitsina, S. Jaiswal, T. Lindh, and J. Sopanen, "General-purpose and scalable internal-combustion engine model for energy-efficiency studies," *Machines*, vol. 10, no. 1, p. 26, Dec. 2021.

[44] O. Tremblay and L.-A. Dessaint, "Experimental validation of a battery dynamic model for EV applications," *World Electr. Vehicle J.*, vol. 3, no. 2, pp. 289–298, May 2009.

[45] R. Khurmi and J. Gupta, *Theory of Machines*. New Delhi, India: Eurasia Publishing House, 2005.

[46] S. Onori, L. Serrao, and G. Rizzoni, *Hybrid Electric Vehicles: Energy Management Strategies*. Cham, Switzerland: Springer, 2016.

[47] S. Jaiswal, M. I. Islam, L. Hannola, J. Sopanen, and A. Mikkola, "Gamification procedure based on real-time multibody simulation," *Int. Rev. Model. Simul.*, vol. 11, no. 5, pp. 259–266, 2018.

[48] R. Niazi, "Generalized modeling approach for real-time simulation," M.S. thesis, Dept. Mech. Eng., Lappeenranta Univ. Technol., Lappeenranta, Finland, 2018.

[49] M. E. Baharudin, A. Rouvinen, P. Korkealaakso, and A. Mikkola, "Real-time multibody application for tree harvester truck simulator," *Proc. Inst. Mech. Eng. K, J. Multi-Body Dyn.*, vol. 228, no. 2, pp. 182–198, 2014.

[50] S. Jaiswal, A. Tarkiainen, T. Choudhury, J. Sopanen, and A. Mikkola, "Gamification and the marketing of agricultural machinery," in *Real-Time Simulation for Sustainable Production: Enhancing User Experience and Creating Business Value*. Evanston, IL, USA: Routledge, 2021.

[51] A. Avello, J. M. Jiménez, E. Bayo, and J. G. de Jalón, "A simple and highly parallelizable method for real-time dynamic simulation based on velocity transformations," *Comput. Methods Appl. Mech. Eng.*, vol. 107, no. 3, pp. 313–339, Aug. 1993.

[52] S. Jaiswal, J. Rahikainen, Q. Khadim, J. Sopanen, and A. Mikkola, "Comparing double-step and penalty-based semirecursive formulations for hydraulically actuated multibody systems in a monolithic approach," *Multibody Syst. Dyn.*, vol. 52, no. 2, pp. 169–191, Jun. 2021.

[53] E. Bayo, J. G. De Jalon, and M. A. Serna, "A modified Lagrangian formulation for the dynamic analysis of constrained mechanical systems," *Comput. Methods Appl. Mech. Eng.*, vol. 71, no. 2, pp. 183–195, 1988.

[54] A. Recuero, R. Serban, B. Peterson, H. Sugiyama, P. Jayakumar, and D. Negrut, "A high-fidelity approach for vehicle mobility simulation: Nonlinear finite element tires operating on granular material," *J. Terramechan.*, vol. 72, pp. 39–54, Aug. 2017.

[55] P. R. Dahl, "A solid friction model," Aerosp. Corp., El Segundo, CA, USA, Tech. Rep. TOR-0158(3107-18)-1, 1968.
[56] S. Jaiswal, J. Sopanen, and A. Mikkola, "Efficiency comparison of various friction models of a hydraulic cylinder in the framework of multibody system dynamics," *Nonlinear Dyn.*, vol. 104, no. 4, pp. 3497–3515, Jun. 2021.
[57] S. Jaiswal, R. Åman, J. Sopanen, and A. Mikkola, "Real-time multibody model-based heads-up display unit of a tractor," *IEEE Access*, vol. 9, pp. 57645–57657, 2021.
[58] F. Mocera and A. Somà, "A review of hybrid electric architectures in construction, handling and agriculture machines," in *New Perspectives on Electric Vehicles*. London, U.K.: IntechOpen, 2021. [Online]. Available: https://www.intechopen.com/chapters/77936, doi: 10.5772/intechopen.99132.
[59] F. Mocera and V. Martini, "Numerical performance investigation of a hybrid eCVT specialized agricultural tractor," *Appl. Sci.*, vol. 12, no. 5, p. 2438, Feb. 2022.
[60] T. A. Burress, S. L. Campbell, C. Coomer, C. W. Ayers, A. A. Wereszczak, J. P. Cunningham, L. D. Marlino, L. E. Seiber, and H.-T. Lin, "Evaluation of the 2010 Toyota Prius hybrid synergy drive system," Oak Ridge Nat. Lab., Oak Ridge, TN, USA, Tech. Rep. ORNL/TM-2010/253, 2011.
[61] J. Nokka, J. Montonen, E. B. Baharudin, P. Immonen, A. Rouvinen, L. Laurila, T. Lindh, A. Mikkola, J. Sopanen, and J. Pyrhönen, "Multibody simulation based development environment for hybrid working machines," *Int. Rev. Model. Simul.*, vol. 8, no. 4, pp. 466–476, 2015.
[62] D. F. Opila, X. Wang, R. McGee, R. B. Gillespie, J. A. Cook, and J. W. Grizzle, "An energy management controller to optimally trade off fuel economy and drivability for hybrid vehicles," *IEEE Trans. Control Syst. Technol.*, vol. 20, no. 6, pp. 1490–1505, Nov. 2011.
[63] L. Tribioli, "Energy-based design of powertrain for a re-engineered post-transmission hybrid electric vehicle," *Energies*, vol. 10, no. 7, p. 918, Jul. 2017.
[64] G. Goswami, S. Jaiswal, C. Nutakor, and J. Sopanen, "Co-simulation platform for simulating heavy mobile machinery with hydraulic actuators and various hybrid electric powertrains," *IEEE Access*, early access, Mar. 3, 2022, doi: 10.1109/ACCESS.2022.3211523.

GIOTA GOSWAMI was born in Agartala, India, in 1992. She received the B.Tech. degree in mechanical engineering from the Kalinga Institute of Industrial Technology, Bhubaneswar, India, in 2014, and the M.S. degree in mechanical engineering from the Lappeenranta-Lahti University of Technology—LUT, Lappeenranta, Finland, in 2019, where she is currently pursuing the Ph.D. degree in mechanical engineering.

From 2014 to 2017, she worked as a Systems Engineer with Tata Consultancy Services Ltd., Kolkata, India. From 2019 to 2020, she was a Research Assistant with the Laboratory of Machine Dynamics, LUT, where she has been working as a Junior Researcher, since 2021. Her research interests include vehicle dynamics, driveline simulations, hybrid powertrains, and multibody dynamics.

ANNA TUPITSINA was born in Saint-Petersburg, Russia, in 1996. She received the B.Sc. and M.Sc. degrees in electrical engineering from Peter the Great St. Petersburg Polytechnical University (SPbPU), Russia, in 2018 and 2020, respectively, and the M.Sc. degree in electrical engineering from the Lappeenranta-Lahti University of Technology—LUT, Lappeenranta, Finland, in 2020, where she is currently pursuing the Ph.D. degree.

From 2018 to 2019, she worked as an Engineer at the Scientific and Technical Center of Unified Power Systems, Saint-Petersburg. Since 2020, she has been working as a Junior Researcher at LUT. Her research interests include simulation and control of hybrid mobile machines.

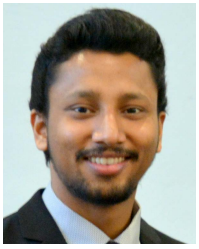

SURAJ JAISWAL was born in Kolkata, India, in July 1991. He received the B.E. degree in production engineering from Jadavpur University, Kolkata, in 2013, and the M.S. and D.Sc. degrees in mechanical engineering from the Lappeenranta-Lahti University of Technology—LUT, Lappeenranta, Finland, in 2017 and 2021, respectively.

From 2013 to 2015, he worked as a Design Engineer with Tata Consultancy Services Ltd., Kolkata, India. Since 2016, he has been working as a Researcher with LUT, where he is currently a Postdoctoral Researcher with the Laboratory of Machine Design. His research interests include multibody dynamics, hydraulic actuators, Kalman filters, friction modeling, and real-time simulation.

Dr. Jaiswal received the "Best Paper Award" at the 9th Asian Conference on Multibody Dynamics (ACMD 2018) held in Xi'an, China, in August 2018. He was awarded a personal grant for his achievements in doctoral studies from LUT Research Foundation, Lappeenranta, in 2021.

CHARLES NUTAKOR was born in Accra, Ghana, in 1982. He received the B.E. degree in plastics technology from the Arcada University of Applied Sciences, Helsinki, Finland, in 2014 and 2018, respectively, and the M.Sc. degree in mechanical engineering and the Ph.D. degree in energy systems from the Lappeenranta-Lahti University of Technology—LUT, Lappeenranta, Finland.

From 2018 to 2020, he worked with the Department of Wind Energy, Technical University of Denmark, as a Postdoctoral Researcher. He rejoined LUT, in 2021, and since has been with the Mechanical Engineering Department as a Postdoctoral Researcher. His current research interests include drivetrains, transmissions, wind turbine loads, drive component dynamics, and lubrication.

TUOMO LINDH was born in Lappeenranta, Finland, in 1964. He received the B.Sc. degree in mechanical engineering from the Mikkeli Institute of Technology, Mikkeli, Finland, in 1989, and the M.Sc. and D.Sc. degrees in technology from the Lappeenranta-Lahti University of Technology—LUT, Lappeenranta, in 1997 and 2003, respectively.

Since 1997, he has been with LUT, where he is currently an Associate Professor. His research interests include generator and motor drives and system engineering, particularly in the areas of distributed power generation, electric vehicles, and mechatronics.

JUSSI SOPANEN (Member, IEEE) was born in Enonkoski, Finland, in 1974. He received the M.S. degree in mechanical engineering and the Ph.D. degree in technology from the Lappeenranta-Lahti University of Technology—LUT, Lappeenranta, Finland, in 1999 and 2004, respectively.

From 1999 to 2006, he worked as a Researcher with the Department of Mechanical Engineering, LUT. From 2004 to 2005, he also worked as a Product Development Engineer at Electric Machine Manufacturer Rotatek Finland Ltd. From 2006 to 2012, he worked as the Principal Lecturer in mechanical engineering and the Research Manager with the Faculty of Technology, Saimaa University of Applied Sciences, Lappeenranta. He is currently working as a Professor in machine dynamics at LUT University. His research interests include rotor dynamics, multibody dynamics, and the mechanical design of electrical machines.